Journal of Applied Physics

Nanoscale plasticity in titania densified alumina ceramics

Cite as: J. Appl. Phys. **131**, 135107 (2022); https://doi.org/10.1063/5.0081872
Submitted: 10 December 2021 • Accepted: 20 March 2022 • Published Online: 07 April 2022

Payel Maiti, Dhrubajyoti Sadhukhan, Jiten Ghosh, et al.

Journal of Applied Physics ARTICLE scitation.org/journal/jap

Nanoscale plasticity in titania densified alumina ceramics

Cite as: J. Appl. Phys. **131**, 135107 (2022); doi: 10.1063/5.0081872
Submitted: 10 December 2021 · Accepted: 20 March 2022 ·
Published Online: 7 April 2022

View Online Export Citation CrossMark

Payel Maiti,[1] Dhrubajyoti Sadhukhan,[2] Jiten Ghosh,[1,a)] and Anoop Kumar Mukhopadhyay[1,3,4,a)]

AFFILIATIONS

[1]XRD and SEM Units, Materials Characterization and Instrumentation Division, CSIR-Central Glass and Ceramic Research Institute, Kolkata 700032, India
[2]Department of Nanoscience and Technology, Central University of Jharkhand, Ranchi 835205, India
[3]Department of Physics, School of Basic Sciences, Faculty of Science, Manipal University Jaipur, Jaipur 303007, Rajasthan, India
[4]Department of Physics, Faculty of Science, Biyani Girls College, Vidhyadhar Nagar, Jaipur 302039, Rajasthan, India

Note: This paper is part of the Special Topic on Advances in Multi-Scale Mechanical Characterization.
[a)]**Authors to whom correspondence should be addressed:** jiten@cgcri.res.in; mukhopadhyay.anoop@gmail.com; and deanscience@biyanicolleges.org

ABSTRACT

The present study explores the physics behind the loading rate (dP/dt or $\dot{P} \approx 1 - 1000\,\mathrm{mN\,s^{-1}}$) dependent nanoscale plasticity (NSP) events observed during carefully controlled nanoindentation (NI) experiments on 1, 3, and 5 wt. % Titania Densified Alumina (TDA) ceramics. Characterizations of the TDA ceramics are carried out by x-ray diffraction, field emission scanning electron microscopy (FESEM), and NI techniques. A significant enhancement (~30%) of the nanohardness of TDA ceramics occur with an enhancement in $\dot{P}$. The results confirm that both the critical load (P_c) at which micro-pop-in or the NSP events initiate and the corresponding critical depth (h_c) are sensitive functions of relative density, size of relatively finer grains, loading rate, and the amount of sintering aids. The experimentally observed empirical power law dependence of all the NSP related parameters on $\dot{P}$ is rationalized theoretically and qualitatively. It is suggested that the shear induced homogeneous dislocation nucleation underneath the nanoindenter may be the main factor contributing to the occurrence of the NSP events at relatively lower loading rates. However, especially at the relatively higher loading rates, the FESEM based evidence and the data obtained from the related NI experiments suggest that there is a more acute interconnection between the homogeneous dislocation nucleation induced profuse occurrence of the NSP events, shear band formations, and microcrack formation in the TDA ceramics. Finally, the design implications of the present results for the development of better alumina ceramics for load and strain tolerant applications are discussed.

I. INTRODUCTION

To face the challenge of expanding application scenarios today, the human civilization requires ever better materials with even higher functional properties and the means to assess if the desired degree of property enhancement is achieved or not. That is why the maximum research focus is currently driven toward the synthesis of better materials with a relatively higher order of functional property enhancement.[1–7] Especially, owing the recent developments in nanoscience, the utilization of a well-known method such as the nanoindentation (NI) technique to assess the situation at the ultrasturctural length scale[8–19] becomes more and more important. Such efforts[1–19] from the recent literature also identify the intimate, important connection between shear induced nanoscale plasticity (NSP) processes such as deformation band formation, slip formation, twinning, etc., as an important means for the material to be able to dissipate energy at the local scale, thereby exhibiting the possibilities of maximum strength enhancement in not only metals and alloys[4–6] but also in ceramics[1–3] and alumina based bulk glasses.[7] In this context, it is interesting to note that the NI technique has been used to understand the structure–property correlation at the ultrastructural length scale of a wide variety of materials, e.g., ion irradiated metals,[8] Al-TiN nanocomposites,[9] VN,[10] Al_2O_3,[11] bulk hBN,[12] high entropy nitrides and carbonitrides,[13] B_6C,[14] HA/TiO_2/CNT nanocomposite,[15] nano-filler

reinforced polymer derived ceramics,[16] 3D printed composites,[17] natural, bicontinuous nanocomposite coating,[18] and $ZnAl_2O_4$–TiO_2 composites.[19] These reports confirm the versatility and capability of the NI technique as a means to assess the intrinsic details of nanoscale deformation not only in ceramics[10–14] and ceramic nanocomposites[9,15,16,19] but also in metals[8] and other composites.[17,18] The current study attempts to use the confluence of these two concepts as it explores the NSP induced hardening observed during the present NI experiments on TDA ceramics.

Alumina, *per se*, is one of the most well-known structural ceramics.[20–23] During sintering, the presence of TiO_2[24] as a sintering aid helps to inhibit grain growth. A survey of literature data (Table I) confirms *that in most of the cases only micromechanical properties are reported for TDA*[25] *and other ceramics.*[26–30] *This is illustrated in the first part of Table I.* The data presented in Table I establishes further that the singular attempt[24] reports only the nanohardness (H_E) and Young's modulus (E) in the case of the 1.68 wt. % TiO_2 densified alumina (TDA) developed by pressureless sintering. *Thus, the physics of nanoscale deformation is yet to be comprehensively understood for the TDA ceramics. This fact serves as the basic scope of and motivation behind the present study.*

The second part of literature survey data presented in Table I of course confirms that in the cases of single alumina grain,[31] single crystalline alumina,[33,34] and polycrystalline alumina,[32,35,36] as well as zirconia toughened alumina (ZTA)[37–39] the *localized NSP events*, i.e., micro-pop-in do occur. The signature of these events in NI experiments mainly occurs in the form of displacement enhancement observed at fixed load and load enhancements observed at fixed displacements. The corresponding load vs depth (P–h) plots exhibit a distinct transition from elastic to plastic deformation. The corresponding load and displacement at which the first micro-pop-in happens are conventionally denoted, respectively, as the critical load (P_c), and the critical depth (h_c).

Thus, depending on applied load of 1000–10 000 μN for single alumina grain, (P_c) varies from ~5 to 30 μN and (h_c) varies from ~0.02 to 2 nm while the nanohardness (H_E) spans the range from 22 to 29 GPa.[31] But at a loading rate of, e.g., 1000 μN s^{-1} a much higher (P_c) of 400 μN and (h_c) of 180 nm are noted for coarse grained (20 μm) alumina,[32] which exhibits (H_E) of 11 GPa and (E) of 300 GPa. For the load range of 0.4–8 mN, the magnitude of (P_c) varies from ~0.4 to 0.58 mN in sapphire which possesses (H_E) of ~27.5 GPa and (E) of ~410–510 GPa.[33] However, when evaluated at a loading rate of 100 μN s^{-1}, the critical load (P_c) in sapphire is reported to be about 50 μN while (H) and (E) values are ~24 and 400 GPa.[34] On the other hand, for an applied (P) range of 0.8–8 mN in the case of the fine (e.g., 0.1 μm) grain alumina; (P_c) spans the range from ~1.2 to 1.5 mN while (h_c) spans the range from 32 to 35 nm. Presumably because of the fine grain size much higher magnitudes of (H_E), e.g., 37–47 GPa, and (E), e.g., 400–620 GPa, are measured.[35] Relatively much higher values of P_c (350 mN) and h_c (1000 nm) are reported for slightly coarse grained (0.9 μm) alumina with a concomitant decrease in (H_E), e.g., about 20 GPa and (E), e.g., about 409 GPa.[36] Similar NSP events are also reported for ZTA ceramics.[37–39]

Thus, the aforesaid survey of literature confirms that in spite of some recent reports[25–30] regarding the micromechanical properties of TDA ceramics, *there is yet to be any systematic study*[24] *at all on their NSP. Furthermore, the study of the simultaneous effect of the loading rate* ($\dot{P}$) *and the variation in the amount of* TiO_2 *sintering aid on the NSP events of pressureless sintered TDA ceramics is not explored till date.* These knowledge gaps define the unique novelty of the present work. Furthermore, the TDA ceramics with 1, 3, and 5 wt. % of TiO_2 as a sintering aid are termed as TDA 1, TDA 3, and TDA 5 ceramics in the current study.

Therefore, the major objective of the current study is to make a comprehensive study of the NSP events exhibited by the micro-pop-ins in the TDA ceramics. The study is done as a function of the loading rate (1–1000 mN s^{-1}) applied during the NI experiments on the TDA ceramics pressureless sintered with various amounts of TiO_2 sintering aid. Furthermore, any possible linkage between the shear deformation band formation and microcrack formation in the TDA ceramics is planned to be studied by extensive usage of the field emission scanning electron microscopy (FESEM) technique.

II. MATERIALS AND METHODS

A. Materials

To prepare the TDA 1, TDA 3, and TDA 5ceramics, 1, 3, and 5 wt. % of TiO_2 powders (>99.9%, Merck, Germany) were mixed in a planetary ball with about 99, 97, and 95 wt. % α-Al_2O_3 (>99.9%, TM-DAR grade, Taimei Chemicals Co. Ltd, Japan) powders, respectively. These powder batches were used to prepare the uniaxially pressed green disks. Finally, the green disks were pressureless sintered at 1600 °C for 2 h in air. The sintered disks had a diameter of ~18.5 mm and a thickness of ~2.5 mm.

B. Methods

The density of the sintered disks was evaluated by Archimedes' principle. A minimum of three to five samples were used to obtain the average values. The compositional details of the TDA ceramics along with their relative density (i.e., ρ_{rTDA}) values are given in Table S1 in the supplementary material. The sintered disks were ground and mirror polished by a grinding machine (Labopol 5, Stuers, Denmark) using diamond pastes of various grit sizes[40] to avoid extraneous influence on the NI results,[41] and the surface roughness (e.g., about 10 nm)[38–40] was measured by a SPM attached to a nanoindenter (Triboindenter, Ti700, Hysitron, USA).[37–39] The phase analysis was done by the XRD technique (ULTIMA IV, Rigaku, Japan; 40 kV, 40 mA, CuK_α, (2θ) : 10°–70°, step size—0.02°). The microstructural analysis was conducted by the FESEM (Sigma, Carl Zeiss, Germany) technique followed by the image analysis technique (Q500MC, Leica, UK) applied to the mirror polished, and subsequently, thermally etched (1500 °C, 1 h, air) disks of the TDA ceramics. The same FESEM technique was used for the examination of the deformation features inside the NI cavities.

Details of the NI experiments have been already reported[34,35,37–40] by us elsewhere, and hence, will not be repeated here. Briefly speaking, all the NI experiments were done at room temperature (~30 °C) and relative humidity ~70% on the mirror polished TDA ceramics by using a nanoindenter (Fischerscope H100-XYp, Fischer, Switzerland) utilizing a diamond Berkovich

TABLE I. Literature scenario of macro-/micromechanical properties of alumina and alumina based other ceramics and composites, sintered with different amount of TiO_2. *h*: depth, *P*: Load, dP/dt: loading rate, P_c: critical load, h_c: critical depth, H_E: experimentally measured hardness, E: experimentally measured Young's modulus, and "–": not reported.

Materials	Sintering aids (TiO_2)	Sintering procedure	*P* (N)	*h* (nm)	dP/dt (μN s^{-1})	H_E (GPa)	E (GPa)	P_c (mN)	h_c (nm)	Reference
Alumina	0.5, 10, and 15 wt. %	Spark plasma	10^6			10.8–12.8, 12.5–13.6, 2.3–2.9				25
ZTA	3 wt. %	Microwave	10			17.68				26
ZTA	3 wt. %	Pressureless	300			15–19				27
Al_2O_3–ZrO_2 ceramic composites	5,10, 15, 20, and 25 mass %	Pressureless	10			5–12.5				28
Alumina–titania coating	13 wt. %	…	1.96			6–9				22
Alumina	0.5, 2, and 4 wt. %	Pressureless	20			19.5–17.5				29
WC-30 vol. % Al_2O_3 composite	2.4 and 6 wt. %	Hot press	300			17.18–14.71				30
Alumina	1.68 wt. %	Pressureless		5000		11, 18, and 17	236, 352, and 303			24
Single alumina grain	…	Pressureless	0.001	…	…	29.03		0.005	0.02	31
Al_2O_3	…	Pressureless	…	…	1000	11	300	0.4	180	32
Sapphire	…	…	0.0004–0.008	…	20–400	27.5	410–510	0.4–0.58 mN	16–22	33
Sapphire	…	Pressureless	…	…	100	24	400	0.05		34
Alumina	…	…	0.0008–0.008	…	…	47–37	400–620	1.2–1.5	32–35	35
Alumina	…	Pressureless and hot isostatic pressing	0.505	1338.1	…	20	409	350	1000	36
10 ZTA	…	Pressureless	0.010–1	…	…	12.1	297	0.115–0.181	1.18–5.11	37
20 ZTA	…	Pressureless	0.010–1	…	…	13.74	464	0.12–0.2	0.87–4.66	38
40 ZTA	…	Pressureless	0.010–1	…	…	13.5	437.64	0.108–0.175	1.1–4.08	39

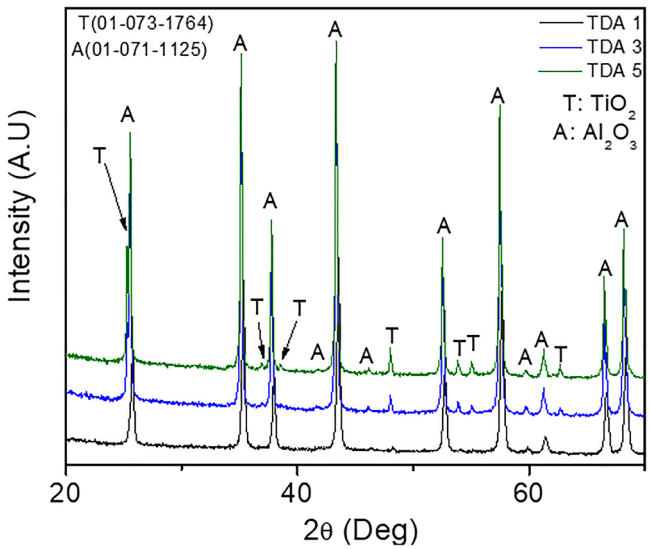

FIG. 1. The XRD pattern of the TDA 1, TDA 3, and TDA 5 sintered ceramics.

nanoindenter of ∼150 nm tip radius (R). Prior to conducting the NI experiment, the machine was calibrated as per the DIN 50359-1 standard following the procedure as already reported[34,35,37–40] by us. The nanohardness (H_E) and Young's modulus data were evaluated from the experimentally obtained load vs displacement (P–h) plots by using the well-known Oliver–Pharr method.[42] The NI experiments were conducted at 14 different but constant loading rates of 1, 1.42, 2, 3.33, 10, 14.2, 20, 33.33, 100, 142.8, 200, 333.33, 500, and 1000 mN s^{-1}. For this purpose, the applied load (P) was fixed at 1000 mN and time (t) was varied from 1 to 1000 s. These loading rates were selected to investigate the entire region of ultra-low and comparatively higher loading rates. After machine calibration, *for each doping level of TiO_2 in the TDA ceramics, NI experiments were done in three samples. For a given loading rate, always the 7 × 7 array of NIs was done in random locations in all the TDA disks.* Thus, each average data for a given sample is actually obtained from 49 times 3, i.e., 147 individual experimental measurements. The data scatter was denoted as ±1 standard deviation.

As (R) is ∼150 nm approximating the actual contact by that between a semi-infinite flat plate and a sphere, the maximum shear stress (τ_{max}), was calculated as[43,44]

$$\tau_{max} = 0.4459\left(\frac{16P_cE_r^2}{9\pi^3R^2}\right)^{\frac{1}{3}}. \quad (1)$$

Here, (E_r) is the reduced modulus.[42] The critical resolved shear stress (τ_{CRSS}) was evaluated as[45]

$$\tau_{CRSS} = \frac{Gb}{4\pi R_D}\ln\left(\frac{R_D}{r_0}\right), \quad (2)$$

where R_D and r_o (∼2b)[45] are the dislocation loop and dislocation core radii while b is Burger's vector. The difference between the corresponding critical loads of two consecutive [e.g., the (n−1)th and (n)th] micro-pop-in events was evaluated as $\Delta P\{=P_{c(n-1)}-P_{c(n)}\}$. The corresponding depth difference is estimated as $\Delta h\{=h_{c(n-1)}-h_{c(n)}\}$. Next, R_D was estimated as[45–47]

$$R_D = \frac{e^1 \times h_L}{8 \times N}. \quad (3)$$

Here, $e^1 = 2.78$ is a constant, h_L (∼G, the grain size)[47] is the characteristic depth, and N (∼$\Delta h/b$)[47] is the number of local dislocation loops active just beneath the nanoindenter. The localized dislocation density (ρ_D) was predicted as $\sim(\pi R_D{}^2)^{-1}$ assuming the area of dislocation loop as $\sim(\pi R_D^2)$.[34] Owing to the dependency of (R_D) on (h) by means of its direct dependency on (Δh) and dependency of (h) on (P), (R_D), and hence, (ρ_D) become the functions of both (h) and (P).

III. RESULTS AND DISCUSSIONS

A. Phase and microstructure analysis

The typical XRD patterns of the TDA ceramics (Fig. 1) confirm the presence of both alumina (A, ICSD code 01-071-1125) and TiO_2 (T, ICSD code 01-073-1764) phases. The FESEM photomicrographs confirm that the microstructures of TDA 1 [Fig. 2(a), relative density 97.2%], TDA 3 [Fig. 2(b), relative density 97.6%], and TDA 5 [Fig. 2(c), relative density 98.3%] are reasonably dense (Table S1 in the supplementary material). Based on the quantitative elemental analysis data (Table II) obtained from the EDAX technique, it is also confirmed that an increase in the amount of Ti happens with an increase in the amount of TiO_2 in the TDA samples, as expected. From the frequency distribution data, the average sizes of coarse grains are about 14.1 ± 1.79 μm for TDA 1 [Fig. 3(a)], 14.03 ± 1.09 μm for TDA 3 [Fig. 3(b)], and 14.11 ± 1.63 μm for TDA 5 [Fig. 3(c)] ceramics, respectively. Similarly, the average sizes of fine grains are about 7.26 ± 0.74 μm for TDA 1 [Fig. 4(a)], 6.28 ± 0.74 μm for TDA 3 [Fig. 4(b)], and 6.13 ± 0.96 μm for TDA 5 [Fig. 4(c)] ceramics, respectively.

B. Nanomechanical responses of the TDA ceramics

The experimental P–h plots for the 14 loading rates ($\dot{P}$) of 1, 1.42, 2, 3.33, 10, 14.2, 20, 33.33, 100, 142.8, 200, 333.33, 500, and 1000 mN s^{-1} for TDA 1 [Fig. 5(a)], TDA 3 [Fig. 5(b)], and TDA 5 [Fig. 5(c)] confirm the significant presence of NSP events characterized by the stochastic occurrence of numerous micro-pop-in events. A detailed discussion of this aspect will be done later in the current study.

The most important observation is that nanohardness and Young's modulus (E) of the TDA ceramics enhance on an average by about 30% [Figs. 6(a)–6(c)] and 28% [Figs. 7(a)–7(c)] with the enhancement in $\dot{P}$. The measured data agree well with those reported literature.[24] It needs to be noted that for pure alumina without any sintering aid for applied loading rates of 1–1000 mN s^{-1}, the magnitude of nanohardness is ∼10.2–12.3 GPa and the magnitude of Young's modulus is ∼295.4–344.3 GPa.[32] Thus, compared to those of pure alumina, a slight improvement in

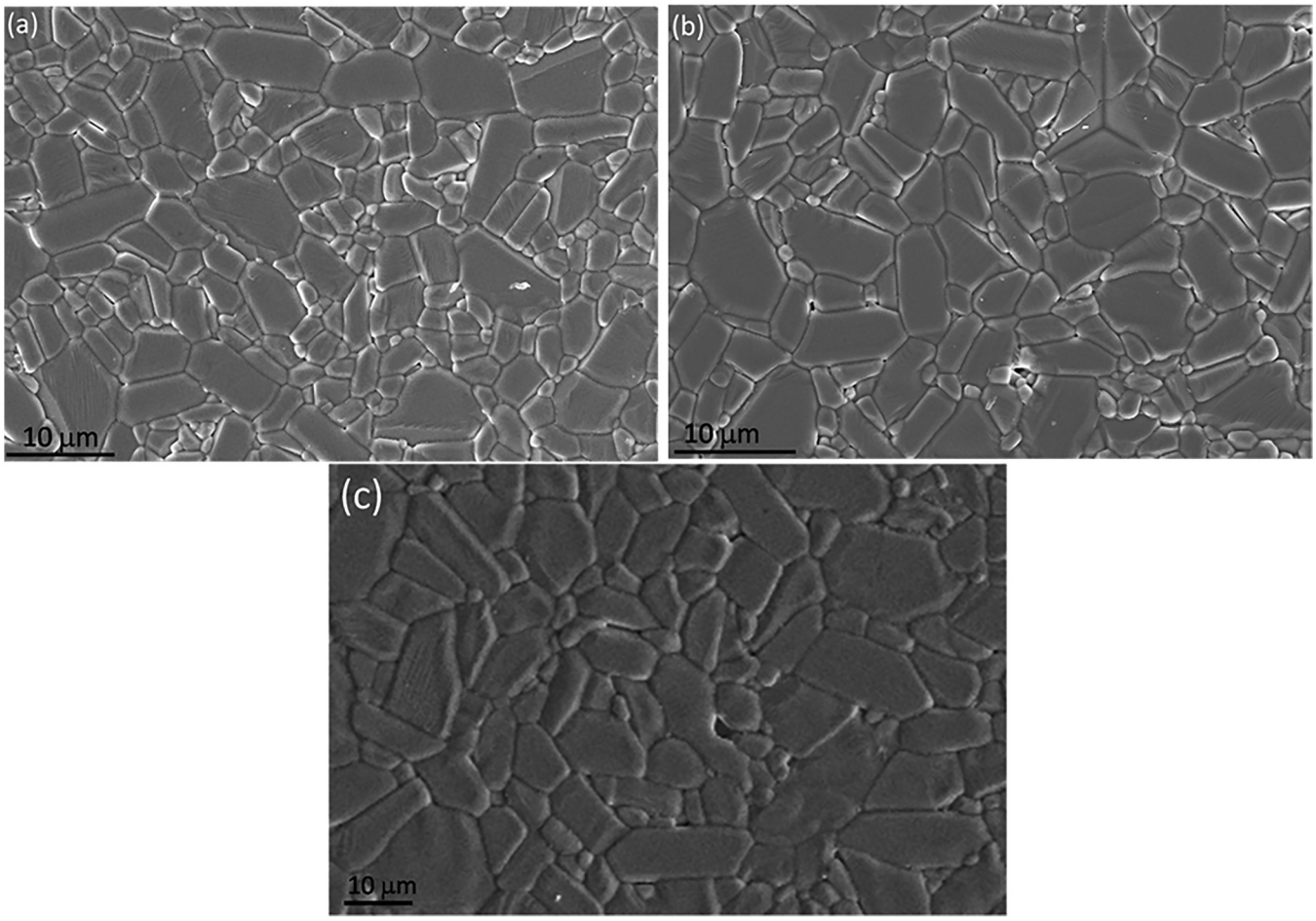

FIG. 2. FESEM photomicrographs of polished and thermally etched disks: (a) TDA 1, (b) TDA 3, and (c) TDA 5.

both nanohardness and Young's modulus occurs in the TDA ceramics.

1. Experimental evidence of NSP in the TDA ceramics

Furthermore, from the enlarged views of the P–h plots, it emerges that there is ample experimental evidence of micro-pop-ins illustrating the NSP events in the TDA ceramics, e.g., Fig. 7(a) (TDA 1, $\dot{P}$–1000 mN s^{-1}), Fig. 7(b) (TDA 3, $\dot{P}$–500 mN s^{-1}), and Fig. 7(c) (TDA 5, $\dot{P}$–100 mN s^{-1}). *The corresponding insets depict the identifications of* (P_c) *and* (h_c) *values for the very first micro-pop-in events*. Although only illustrative examples are included in Figs. 7(a)–7(c) for the sake of brevity, similar instances are valid at all the loading rates considered in the current study.The typical illustraive examples of (ΔP) and (Δh) are shown in Fig. 8(a) (TDA 1, $\dot{P}$–13.33 mN s^{-1}), Fig. 8(b) (TDA 3, $\dot{P}$–10 mN s^{-1}), and Fig. 8(c) (TDA 5, $\dot{P}$–2 mN s^{-1}).

TABLE II. Quantitative elemental analysis of TDA samples.

Sample	C (at. %)	Al (at. %)	Ti (at. %)	O (at. %)
TDA 1	11.1	38.6	0.2	50.1
TDA 3	13.1	37.5	0.3	49.1
TDA 5	16	38	0.5	45.5

2. The power law dependency

For the TDA 1 ceramics, the empirical power law dependencies of (P_c), (h_c), (ΔP), and (Δh) on $\dot{P}\left(=\frac{dP}{dt}\right)$ are shown in Figs. 9(a)–9(d), respectively. Similarly, the empirical power law dependencies of (τ_{max}), (ρ_D), (R_D), and (τ_{CRSS}) on $\dot{P}$ are shown in turn in Figs. 10(a)–10(d) for the TDA1 ceramics. Furthermore, in the cases of TDA 3 and TDA 5 ceramics, the empirical power law dependencies of all the NSP related parameters on $\dot{P}\left(=\frac{dP}{dt}\right)$ are shown in correspondence in Figs. S1–S4 in the supplementary material. Except for the case of (R_D) which bears a negative trend [Figs. 10(c) and

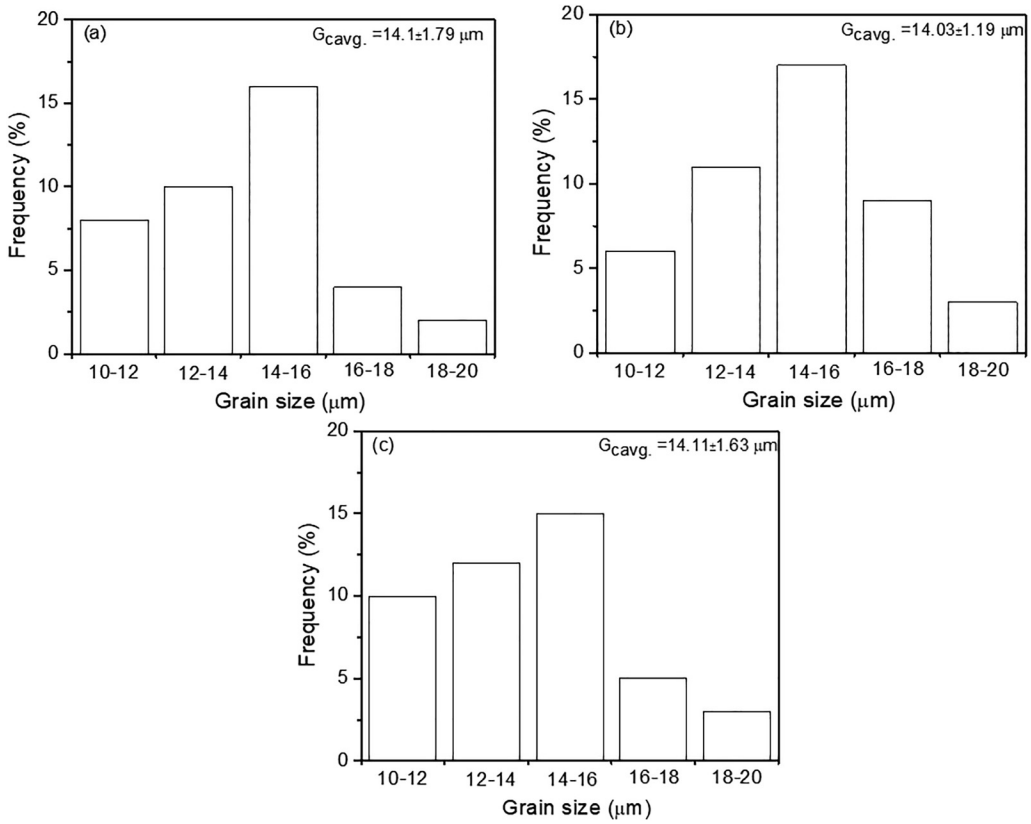

FIG. 3. Grain size distribution plots of coarse alumina grains for sintered disks: (a) TDA 1, (b) TDA 3, and (c) TDA 5.

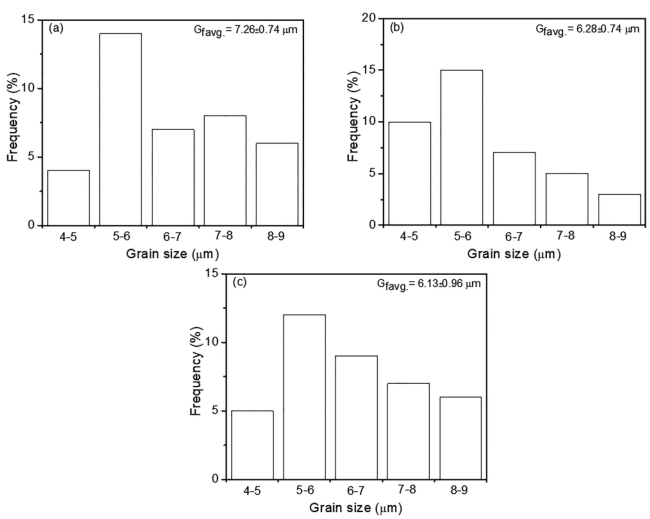

FIG. 4. Grain size distribution plots of fine alumina grains for sintered disks: (a) TDA 1, (b) TDA 3, and (c) TDA 5.

S2(c) and S4(c) in the supplementary material], all other quantities exhibit empirical power law dependencies with positive exponents on the loading rate [Figs. 9(a)–9(d), 10(a), 10(b), and 10(d), S1(a)–S1(d), S2(a), S2(b), S2(d), S3(a)–S3(d), S4(a), S4(b), and S4(d) in the supplementary material].

Beyond a threshold loading rate ($\dot{P}_{Th}$) of, e.g., 33.3 mN s^{-1}, a definite change of slope occurs in all cases, Figs. 9 and 10 and S1–S4 in the supplementary material. Furthermore, for all ($\dot{P} > \dot{P}_{Th}$), the slope increases. These facts suggest a possible change in the mechanism of deformation. Here, the results of power law fitting in the two regimes of loading rates, e.g., 1–33.3 mN s^{-1} and 33.3–1000 mN s^{-1}, are shown for the TDA 1, TDA 3, and TDA 5 ceramics in Tables III, S2, and S3 in the supplementary material, respectively. The goodness of fitting (R^2) in most of the cases is ≥0.9 and even as high as 0.95–0.99. Therefore, it seems plausible to argue that the empirical power law equations proposed in the current study represent the trend of the experimental data correctly. It has been suggested[32] that at higher $\dot{P}$, the rate of energy transfer to alumina may be much faster as compared to that at lower $\dot{P}$. It may, thus, enhance the localized compressive strain, and hence, the compressive stress (σ_c). If this picture is correct, then at higher $\dot{P}$,

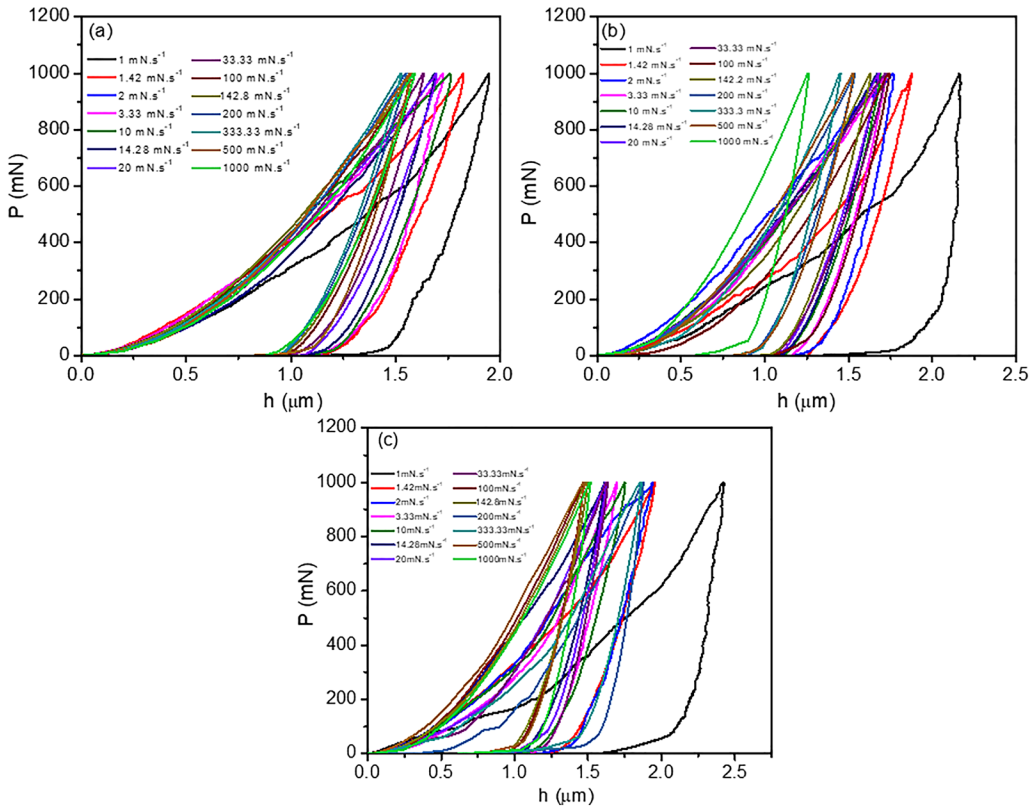

FIG. 5. Load (P) vs depth (h) plots at different loading rates from 1 to 1000 mN s^{-1} for (a) TDA 1, (b) TDA 3, and (c) TDA 5 ceramics.

a higher P_c should be required to initiate the NSP events afresh. The current experimental data match with this picture.

3. Justification of empirical power law dependencies

Even in the case of single crystal alumina, an empirical power law dependency of (P_c) on ($\dot{P}$) with positive exponent occurs.[34] Now, (h_c) is directly related to (P_c) which has a power law dependency on ($\dot{P}$). Therefore, (h_c) depends on ($\dot{P}$) through a power law form. In addition, (ΔP) depends on (P_c). But (P_c) bears a power law dependency on ($\dot{P}$). Hence, (ΔP) is dependent on ($\dot{P}$) through a power law. Furthermore, (Δh) is a function of (h_c) which bears empirical power law dependency on ($\dot{P}$). Thus, (Δh) exhibits a power law dependency on ($\dot{P}$). On the other hand, (τ_{max}) has power law dependency on (P_c) which bears a power law dependency on ($\dot{P}$). Therefore, (τ_{max}) exhibits power law dependency on ($\dot{P}$). Further, (ρ_D) is related to $(R_D)^{-2}$ where in (R_D) is inversely proportional to Δh [Eq. (3)] which has a positive power law dependency on ($\dot{P}$). Therefore, it follows that (R_D) depends on ($\dot{P}$) with a negative exponent. Due to this fact, (ρ_D) exhibits a positive power law dependency on ($\dot{P}$). Further, (τ_{CRSS}) is inversely related to (R_D) which bears a negative power law dependency on ($\dot{P}$). Hence, (τ_{CRSS}) shows power law dependency with positive exponent on ($\dot{P}$). Thus, the data presented in Figs. 9 and 10, and S1–S4 in the supplementary material and Tables III, S2, and S3 in the supplementary material for the TDA 1, TDA 3, and TDA 5 ceramics are rationalized. Further, it is interesting to note that for 20 μm grain size of alumina, (P_c) increases from 0.4 to 30 mN when ($\dot{P}$) increases from 10^3 to 10^6 μN s^{-1}.[32] Similarly, (P_c) increases from 6 to 300 μN when ($\dot{P}$) increases from 10^1 to 10^4 μN s^{-1} for sapphire.[34] Thus, the current data trend observed for the TDA ceramics matches with those reported already in the literature for coarse grain polycrystalline[32] and single crystalline[34] alumina ceramics. This aspect shall be further discussed in this study.

4. The role of shear stress in micro-pop-in events of the TDA ceramics

In loading rate dependent micro-pop-in events in the TDA ceramics, the magnitude of τ_{max} developed just beneath the nanoindenter is ~14.82–78.02 GPa for TDA 1 [Fig. 10(a)], 14.71–78 GPa for TDA 3 [Fig. S2(a) in the supplementary material], and 14.6–75.14 GPa for TDA 5 sintered ceramics [Fig. S4(a) in the supplementary material].Thus, the average τ_{max} values of 27.87, 28.32, and 29.57 GPa are evaluated for the TDA 1, TDA 3, and TDA 5 ceramics. These τ_{max} values are much higher than theoretical shear strength (τ_{theo}) of ~2.97, 2.91, and 2.85 GPa estimated for the TDA 1, TDA 3,

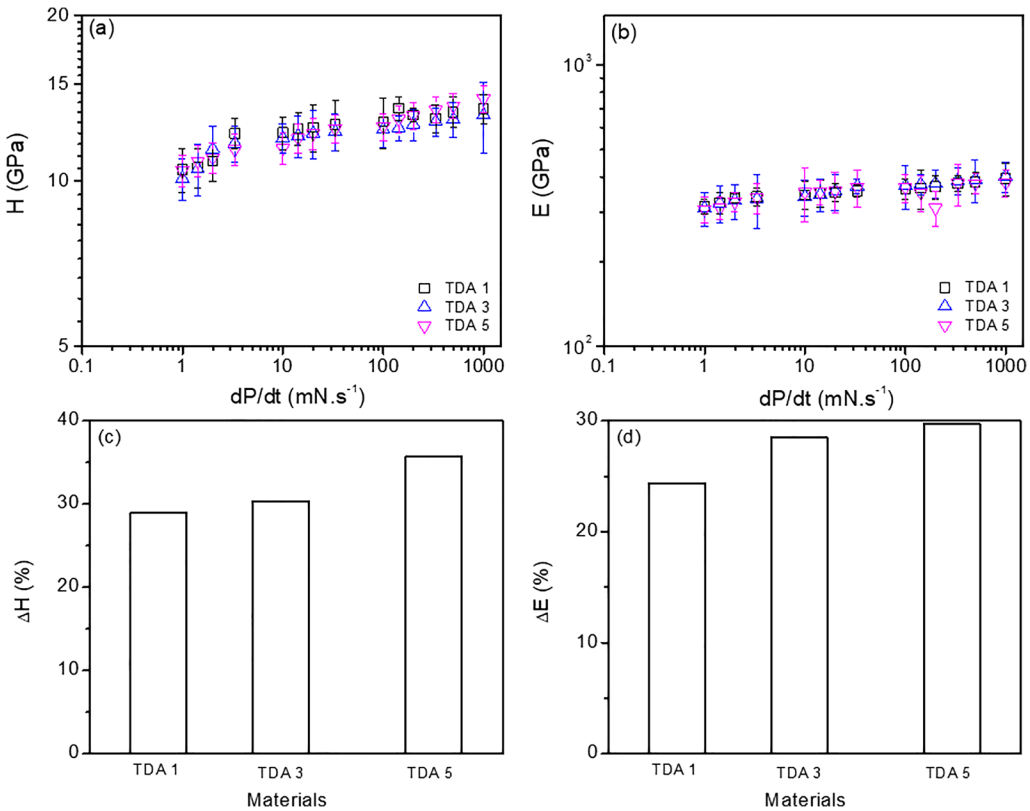

FIG. 6. Variations of (a) nanohardness (H) and (b) Young's modulus (E) with the loading rates (dP/dt) for all TDA samples. Variations of % change of (c) nanohardness (ΔH %) and (d) Young's modulus (ΔE %) with the wt. % change of sintering aid TiO_2 in alumina ceramics.

and TDA 5 ceramics, respectively. *The magnitude of* (τ_{theo}) *of the TDA ceramics was estimated by the conventional, well-known rule of mixture,* e.g., $t_{theo\ TDA} = [(t_{theo\ Al_2O_3}.wt.\%_{Al_2O_3}) + (t_{theo\ TiO_2}.wt.\%_{TiO_2})]$. *Here,* $wt.\%_{Al_2O_3}$ *denotes the wt. % of* Al_2O_3 *and wt%* $_{TiO_2}$ *denotes the wt. % of* TiO_2. *For this purpose, the magnitude of* ($\tau_{theoAl_2O_3}$) *is taken as ~3 GPa for polycrystalline alumina.*[45,48] *However, the magnitude of* ($\tau_{theo\ TiO_2}$) *is taken from Ref.* 49 *as ~340 Pa.*

For a perfect crystal, the theoretical shear strength is ~G/30 to G/5 where G refers to the shear modulus.[50–53] The NSP or initial stage of plastic deformation occurs due to dislocation nucleation after crossing this limit of theoretical shear strength.[50] If the magnitude of maximum shear stress locally active beneath the nanoindenter becomes ≥the theoretical shear strength, the micro-pop-in happens.[47] Furthermore, the value of maximum shear stress was found[35] to be of the order of theoretical shear strength (~G/30 to G/5),[50] i.e., 28–30 GPa which exactly matches with the average τ_{max} values of 27.87, 28.32, and 29.57 GPa evaluated, respectively, for the TDA 1, TDA 3, and TDA 5 ceramics. As (τ_{max}) is ≫(τ_{theo}), it is expected[31–35,45–47] that shear deformation bands may form inside the NI impression. The actual experimental evidence in support of this suggestion is provided below.

5. Evidence of shear induce deformations in micro-pop-in events of the TDA ceramics

As a typical illustrative example, for $\dot{P}$ of 33.33 mN s^{-1}, the formations of shear deformation bands inside the NI cavities are confirmed from the bunch of FESEM images [TDA 1, Figs. 11(a) and 11(b)], [TDA 3, Figs. 12(a) and 12(b)], and [TDA 5, Figs. 13(a) and 13(b)]. For the TDA1 ceramic, the portion marked as "A" in Fig. 11(a) contains five shear deformation bands. The corresponding portion in exploded view is clearly shown in Fig. 11(b). The separations between two successive shear deformation bands are 210, 267, 265, 175, and 207 nm for the region "D," "E," "F," "G," and "H," respectively. So, the average separation between two successive shear deformation bands is ~224.8 ± 40 nm. Similarly, for the TDA 3 ceramics, the shear deformation bands are formed inside the NI cavity, in the region marked as "I" in Fig. 12(a). The corresponding portion in exploded view is clearly shown in Fig. 12(b). It depicts three shear bands, marked as "K," "L," and "M." The separations between two successive shear bands are 186, 233, and 198 nm, respectively. Here, the average separation between two successive shear deformation bands is decreased to, e.g., ~205.6.5 ± 24.1 nm. In a similar manner, for the TDA 5 ceramics, the exploded view of the portions marked as "P" and "N" in Fig. 13(a) is shown in

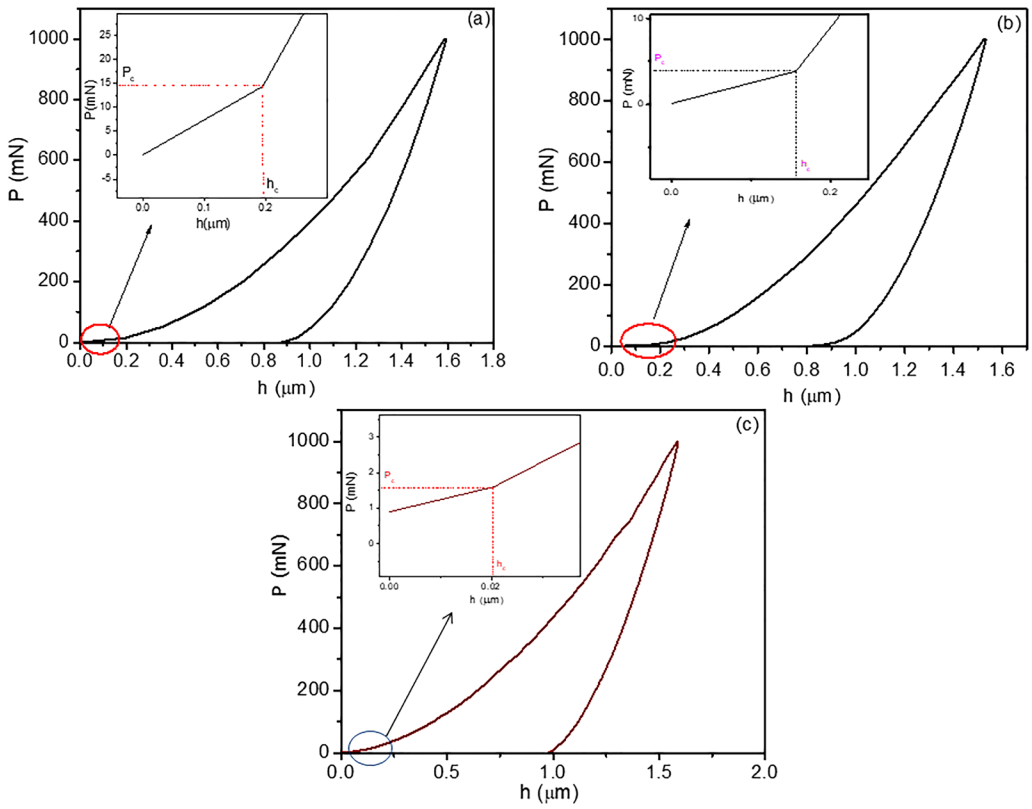

FIG. 7. The typical P–h plot at loading rate: (a) 1000 mN s^{-1} for TDA 1, (b) 500 mN s^{-1} for TDA 3, and (c) 100 mN s^{-1} for TDA 5 ceramics. The insets show the very first critical load (P_c) and corresponding critical depth (h_c).

Fig. 13(b). The shear band locations corresponding to the region "P" are marked as "S," "T," and "U" while those corresponding to the region "N" are marked as "X" and "Y." The portion "P" contains three shear deformation bands with separations of 275, 181, and 150 nm. Hence, the average separation between two successive shear deformation bands is ~202 ± 65 nm for the region marked as "P." Furthermore, there are two shear deformation bands in the portion "N." The separations between the successive shear bands are 287 and 193 nm in the region "N." Thus, the average separation between two successive shear deformation bands is ~240 ± 66.4 nm for the region "N." So, the grand average separation between two successive shear deformation bands is about 218.1 ± 45.2 nm for the current TDA ceramics. However, the data match well with the reported data range, e.g., (50–5000 nm)[37–39,45,48,54–58] for polycrystalline and single crystalline alumina, alumina zirconia composites, bulk metallic glass, etc. The interband separation of shear deformation bands depends on several factors such as whether the structure is crystalline or not,[48] the microstructure is polycrystalline or single crystalline,[37–39] local microstructural flaws,[45] and residual stress.[54–58] Thus, based on the formation of shear bands inside the NI cavity [Figs. 11(a), 11(b), 12(a), 12(b), 13(a), and 13(b)], the fact that τ_{max} is $\gg \tau_{theo}$, estimated values of high dislocation density [Figs. 10(b), S2(b), and S4(b) in the supplementary material] and literature evidence,[31–35,59,60] it seems plausible to argue that two factors, i.e., nucleation of dislocation and shear *deformation band formations* may be simultaneously responsible for the genesis of NSP events in the present TDA ceramics.

6. The linkage of NSP events with the microcrack formation in the TDA ceramics

As far as experimental evidence is concerned, it is a fact that along with shear deformation band formations, microcracks also form. These microcracks form at/near the vertices of the nanoindents. Typical illustrative examples of these are shown in Figs. 11(a), 12(a), and 13(a) for the TDA 1, TDA 3, and TDA 5 ceramics, respectively, for $\dot{P}$ of 33.33 mN s^{-1}. Thus, using black dotted elliptical areas, the microcracks are denoted by "B" and "C" in Fig. 11(a) for the TDA 1 ceramics. Further, in the case of the TDA 3 ceramics, black dotted elliptical area "J" is utilized to depict the microcrack in Fig. 12(a). In a similar way, for the TDA 5 ceramics, black dotted elliptical areas denoted by "Q" and "R" are used to mark the microcracks, Fig. 13(a). The microcrack formation helps the ceramic to be locally more compliant. It is well-known[32] that if the magnitude of critical resolved shear stress (τ_{CRSS}) $\ll \tau_{max}$, the microcracks can

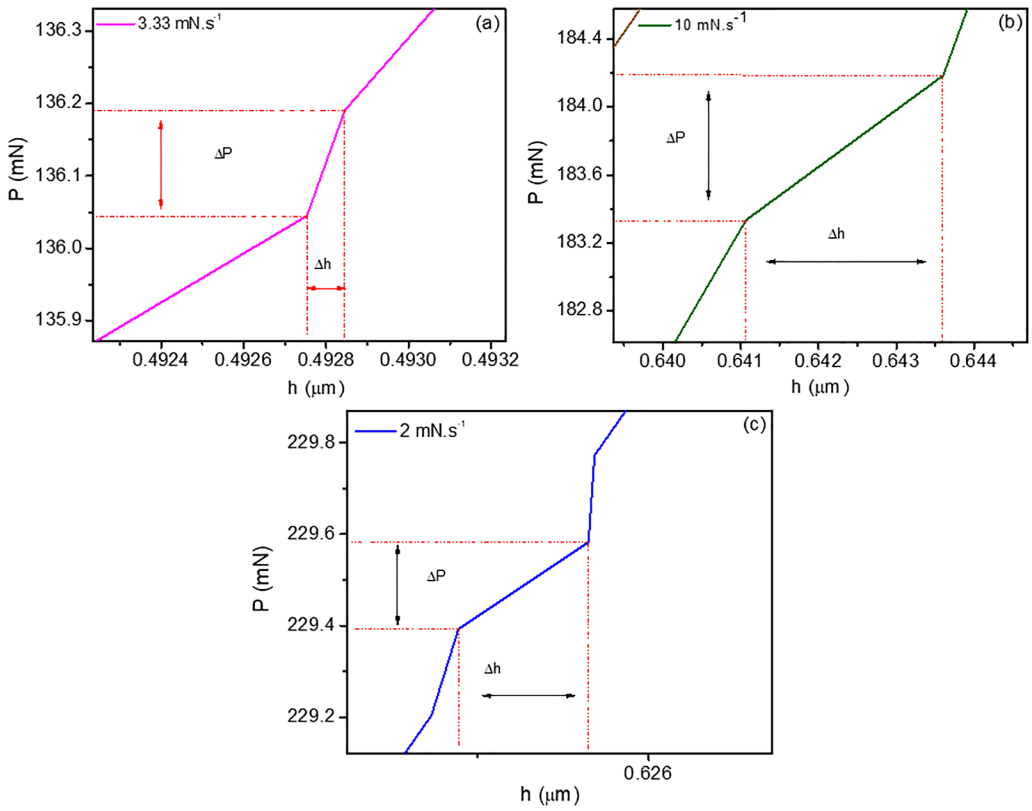

FIG. 8. Exploded views of typical P–h plots showing serration or micro-pop-in events, at loading rates (a) 3.33 mN s^{-1} for TDA 1, (b) 10 mN s^{-1} for TDA 3, and (c) 2 mN s^{-1} for TDA 5 ceramics.

form very easily. Indeed, the values of (τ_{CRSS}) estimated by Eq. (2) are very small, e.g., ~0.15–5.48 GPa for the TDA 1 [Fig. 10(d)], 0.22–5.8 GPa for the TDA 3 [Fig. S2(d) in the supplementary material], and 0.15–6.1 GPa for the TDA 5 ceramics [Fig. S4(d) in the supplementary material]. In fact, these values are much smaller than the average τ_{max} values of 27.87, 28.32, and 29.57 GPa evaluated for the TDA 1, TDA 3, and TDA 5 ceramics, respectively. Such a situation helps in the formation of the microcracks as illustrated in Figs. 11(a), 12(a), and 13(a). Based on the aforementioned experimental evidences and theoretical justifications,[32,48] *it is suggested that there is a connection between the occurrence of NSP events and localized shear band formations as well as microcrack formations in the TDA ceramics*. The issue of the relative contributions of shear band formation and microcrack formation to the NSP events in the TDA ceramics is very important to understand. Therefore, it is decided to discuss it separately later in the present study.

7. The influence of sintering aid on nanomechanical responses of the TDA ceramics

The relative density (Table S1 in the supplementary material) and coarse grain size (Fig. 3) of the TDA ceramics slightly increase with the enhancement in the amount of TiO_2 that is used as a sintering aid. The amount of Ti in the microstructure is also shown to be increased in the TDA ceramics as the amount of sintering aid is increased (Table II). Concomitantly, the fine grain size decreases (Fig. 4) with the enhancement in the amount of TiO_2 used as the sintering aid. The relative density increases as a more solid solution of TiO_2 in Al_2O_3 happens.[61] The EDAX analysis data presented in Table II work support this view. Simultaneously, the cation vacancy increases in the TDA ceramics. This leads to slight enhancement in coarse grain size.[61] Further, as the total sample volume is fixed, due to simultaneous increase in density and coarse grain size, there is a decrease in fine grain size of the TDA ceramics. In order to study the effect of sintering aid on the NSP events of the TDA ceramics, the values of critical load (P_c) for some selected loading rates are plotted in Fig. 14. For a very rough comparison purpose only, an alumina sample (e.g., grain size about 20 μm, relative density about 95% of theoretical) developed earlier[48] without any sintering aid using the same alumina powder at the similar sintering conditions as used in the present work is also characterized and the corresponding values of P_c are incorporated in Fig. 14. For this comparison, the loading rates of, e.g., 3.33, 33.3, 500, and 1000 mN s^{-1}, are selected such that they may represent the trend of results in both lower and higher loading rate regions. It is evident from the data

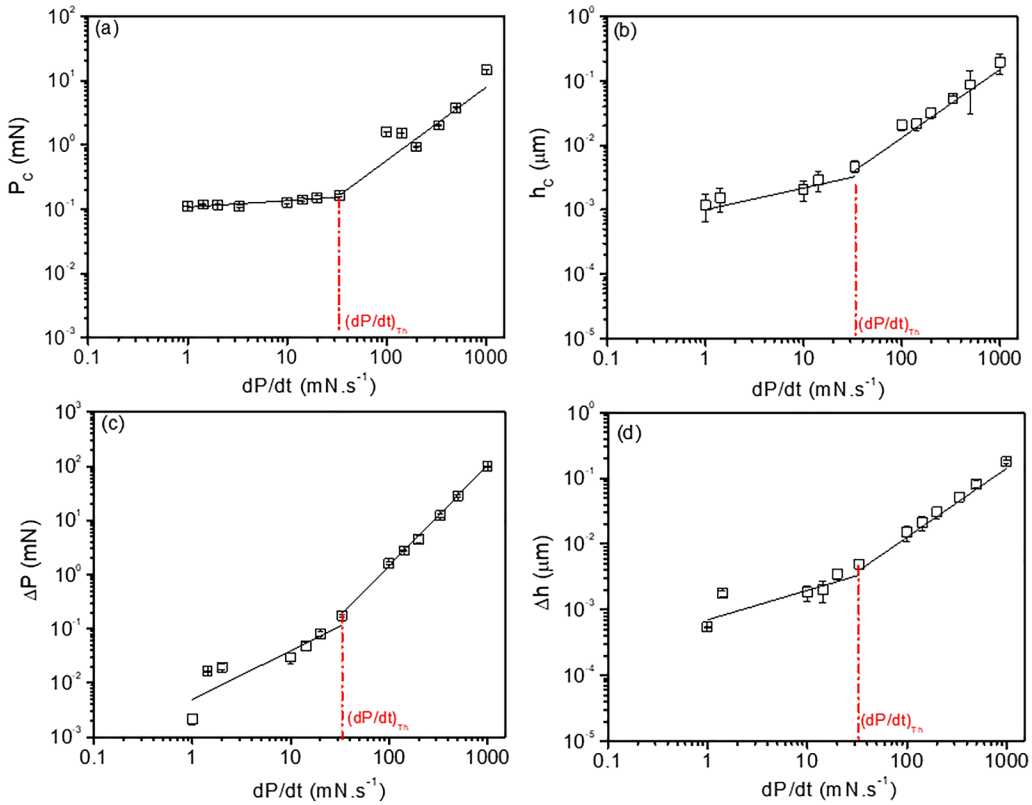

FIG. 9. Variations of (a) P_c, (b) corresponding h_c, (c) ΔP, and (d) Δh showing positive power law dependencies on (dP/dt) for the TDA 1 ceramics.

plotted in Fig. 14 that for a given loading rate, the values of P_c is lowest for the undoped alumina and thereafter it continuously increases slightly as the amount of sintering aid increases. The alumina sample has a higher grain size, lower relative density, and hence, the lowest value of P_c. Since there was no sintering aid, the grain size was uncontrolled and the densification was not as good as in the TDA ceramics. However, the trend of increase in (P_c) with the amount of sintering aid becomes relatively more prominent at higher loading rates. At a higher loading rate, more energy is driven into the system per unit time. It makes the system locally and temporarily more resilient. Hence, the critical load to initiate the first NSP event assumes a relatively higher value in a given TDA ceramic at a given higher loading rate. As the microstructure becomes denser and finer with the increase in the amount of sintering aid, it becomes more and more difficult to initiate the localized NSP events at a given loading rate. Therefore, the magnitude of (P_c) increases with the amount of sintering aid in the TDA ceramics.

8. Note on theoretical justification of the current observations

Based on the theoretical work published earlier by us[32,48] and other researchers,[62] the instantaneous infinitesimal small load (δP) and corresponding depth (δh) recorded during the loading cycle of a given NI experiment can be related by an empirical power law function as

$$\delta P = S(\delta h)^q. \tag{4}$$

Here, S is the pre-exponential factor is an empirical constant and q is the power law exponent $(0 < q < 2)$.[62]

Thus, the time derivatives are related as

$$\dot{\delta P} = Fq(\delta h)^{q-1}\dot{\delta h} \approx Fq(\delta h)^{q-1}G.$$

As $\dot{\delta h}$ is negligibly small[32,48] in general in alumina ceramics, e.g., about few nm s^{-1} assuming it approximately as a constant G, we have, with another constant $I = FG$,

$$\dot{\delta P} = Iq(\delta h)^{q-1},$$

or,

$$\delta h = (Iq)^{-\gamma}\dot{P}^{\gamma} = T\dot{\delta P}^{\gamma}. \tag{5}$$

Here, $\gamma = (q-1)^{-1}$ and $T = (Iq)^{-\gamma}$ is another constant. Thus,

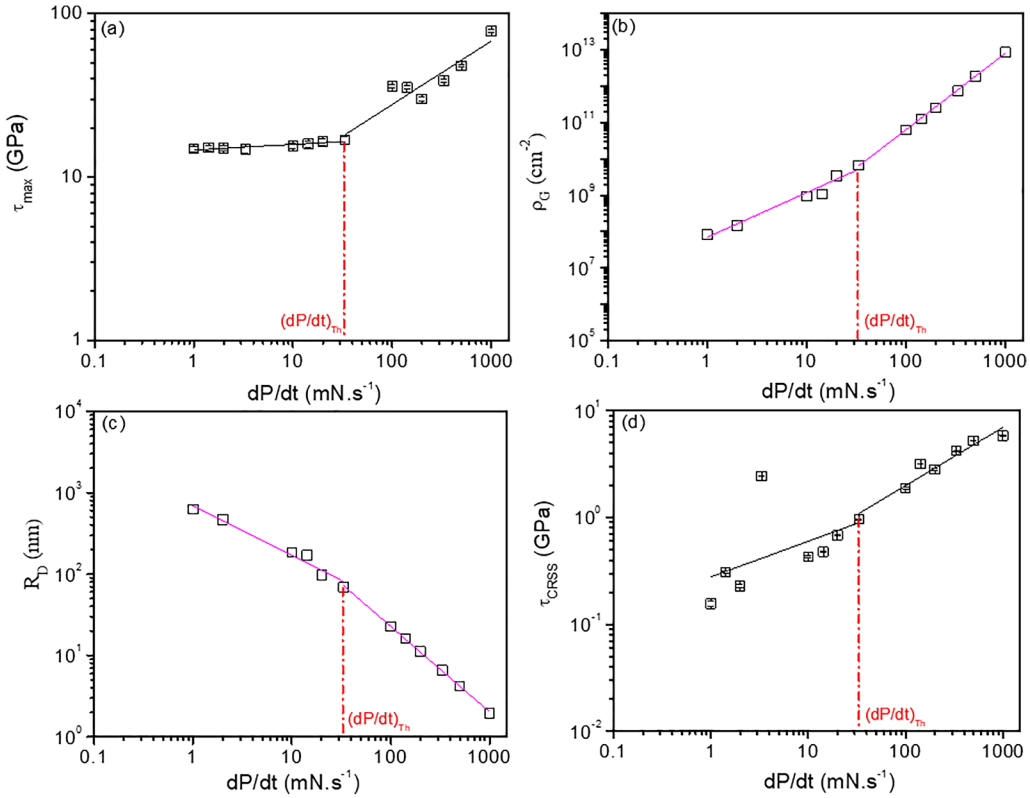

FIG. 10. Variations of (a) (τ_{max}), (b) (ρ_D) per unit area, (c) (R_D), and (d) (τ_{CRSS}) showing power law dependence on (dP/dt) in the case of the TDA 1 ceramics.

Eq. (5) suggests an empirical power law dependency of depth (δh) on the loading rate, $\dot{\delta}P$. But, from Eq. (4),

$$\delta h = (\delta P S^{-1})^{\left(\frac{1}{q}\right)} = (\delta P S^{-1})^{(\varepsilon)}. \tag{6}$$

Here, $\epsilon = (q)^{-1}$. Thus, eliminating δh between Eqs. (5) and (6), we have

$$\delta P = L(\dot{\delta}P)^n. \tag{7}$$

Here, the pre-exponent term [L) is given by $[S(T)^q]$ and the power law exponent, $n = \gamma q$. Equation (7) exhibits an empirical power law dependence of load on the loading rate, $(\dot{\delta}P)$. It needs to be recognized that the critical load (P_c) is also a load value. Hence, its empirical power law dependency on the loading rate is expected. The same is indeed experimentally observed in the data plots of the present study [Figs. 9(a), S1(a), and S3(a) in the supplementary material]. Similarly, the critical depth (h_c) is also a depth value. Therefore, its empirical power law dependency on the loading rate is expected. The same trend is indeed experimentally observed from the data of the present study (Figs. 9 and 10, and S1–S4 in the supplementary material). In the cases of the TDA 1 ceramics (Table III), TDA 3 ceramics (Table S2 in the supplementary material), and TDA 5 ceramics (Table S3 in the supplementary material), the values of (L) and (n) from the current study have an order of magnitude match with those reported in the literature for NI of alumina,[32,34,35] thereby giving further credence to the current observations regarding power law dependencies of the NI related parameters on the loading rate regimes in correspondence.

A very recent study on the NI of (100) as well as (111) surfaces of BCC Fe and (100) surface of FCC Cu provides undeniable evidence about the power law dependencies of corresponding loads (P_{pop-in}) at micro-pop-in events on loading rates $\dot{P}\left(=\frac{dP}{dt}\right)$. These results also follow the prediction made through analytical atomistic modeling and MD simulations[63,64] as given below:

$$P_r^{(P_{pop-in})} = \frac{D_{NR}(P_{pop-in})exp\left[-(dP/dt)^{-1}\int_0^{P_{pop-in}} D_{NR}(P)dP\right]}{\int_0^{P_{cpop-in}} D_{NR}(P_{pop-in})exp\left[-(dP/dt)^{-1}\int_0^{P_{pop-in}} D_{NR}(P)dP\right]dP_{pop-in}}. \tag{8}$$

In Eq. (8),[63,64] $P_r^{(P_{pop-in})}$ represents the probability of occurrence of a micro-pop-in event, D_{NR} is the dislocation nucleation rate, and $P_{cpop-in}$ stands for the maximum magnitude of the pop-in load at which the cumulative probability for the occurrence of the pop-in event approaches 1.[63,64] A similar equation is yet to be available for brittle polycrystalline ceramics. However, such a physical

TABLE III. Summary of the empirical power law equations, the pre-exponential factors (L), the power law exponential factors (n), and goodness of fitting (R^2) obtained for the micro-pop-in related parameters as obtained from the experimental data for the lower loading rate (1–33.3 mN s^{-1}) and higher loading rate (33.3–1000 mN s^{-1}) regime of the TDA 1 ceramics.

Empirical power law equations of micro-pop-in parameters for TDA 1 ceramics							
(dP/dt = 1–33.3 mN s^{-1})				(dP/dt = 33.3–1000 mN s^{-1})			
Equations	(L)	(n)	(R^2)	Equations	(L)	(n)	(R^2)
$P_c = 0.107(dP/dt)^{0.103}$	0.107	0.103	0.84	$P_c = 0.003(dP/dt)^{1.14}$	0.003	1.14	0.88
$h_c = 0.001(dP/dt)^{0.338}$	0.001	0.338	0.90	$h_c = 0.0001(dP/dt)^{1.058}$	0.0001	1.058	0.99
$\Delta P = 0.005(dP/dt)^{0.896}$	0.005	0.896	0.81	$\Delta P = 0.0003(dP/dt)^{1.845}$	0.0003	1.845	0.99
$\Delta h = 0.0007(dP/dt)^{0.448}$	0.0007	0.448	0.85	$\Delta h = 0.0001(dP/dt)^{1.051}$	0.0001	1.051	0.99
$\tau_{max} = 14.64(dP/dt)^{0.034}$	14.64	0.034	0.84	$\tau_{max} = 4.66(dP/dt)^{0.388}$	4.66	0.388	0.87
$\rho_{GND} = 7 \times 10^7(dP/dt)^{1.229}$	7×10^7	1.229	0.97	$\rho_{GND} = 4 \times 10^6(dP/dt)^{2.102}$	4×10^6	2.102	0.99
$R_D = 690.2(dP/dt)^{-0.61}$	690.2	−0.61	0.97	$R_D = 2858(dP/dt)^{-1.05}$	2858	−1.05	0.99
$\tau_{CRSS} = 0.185(dP/dt)^{0.421}$	0.185	0.421	0.90	$\tau_{CRSS} = 0.161(dP/dt)^{0.546}$	0.161	0.546	0.94

situation depicts a statistical distribution of the corresponding load values as an intrinsic characteristic of the NSP events. This aspect is discussed next with further details.

9. Relative contribution of the shear band formation and microcrack formation in the NSP events in the TDA ceramics

Several researchers report the occurrence of shear induced NSP events (e.g., micro-pop-in) and microcrack formation in A-, R-, C, and M-planes of single crystal alumina,[65] polycrystalline alumina,[32] ZTA ceramics,[38–40] single crystals of $SrTiO_3$, $BaTiO_3$, TiO_2, and α-alumina,[66] and iron oxide based nanocomposites.[67] However, because of the intrinsically stochastic nature[65] of these small scale events, an exact quantification of how much could be the relative contributions of shear induced deformation band formation and microcrack formation to the characteristic NSP events is yet to be available across the wide variety of materials[32,38–40,65–67] including the case of the present TDA ceramics. Nevertheless, there is no denial that it is one of the most pertinent problems for researchers to tackle.

In the principle course, it is highly appreciable that there should be a critical tip radius (R_{cr}), and hence, critical contact stress below which the deformation will be dislocation dominated and above which it will be microcrack dominated. The major difficulty lies in setting up the appropriate boundary conditions to end with a closed form solution for the tip radius value which will, in turn, affect the contract stress value that matters the most, especially for brittle ceramics like alumina. This is because the boundary conditions, in reality, will involve a multitude of relevant factors. These boundary conditions are suggested[66] to be linked to, e.g., different deformation mechanisms, existing slip systems in the material at the test temperature, the presence or absence of lattice friction stress, the magnitude of the Burger's vector, etc. Furthermore, it may be linked[66] to the statistical distribution and surface density of pre-existing defects induced by the grinding and polishing processes, the humidity of test ambience, the presence or absence of surface reactivity as well as oxidizing and reducing atmosphere. Furthermore, it could be connected[66] to variations in the loading rate, relative stiffness of the nanoindenter tip, etc. In addition when the concurrent occurrence of plastic deformation and microcrack formation happens for nanoindenter tips with a large radius, it is opined[66] to be extremely difficult to identify the exact sequence of plastic deformation dominated NSP event and microcrack dominated NSP events.

There is, so far, only a singular success in the case of a "pre-existing-crack free" $SrTiO_3$ single crystal.[68] This study identifies that the sequence of events could be a stage of elastic deformation followed by dislocation activation on primary slip planes. The slip planes will need to be inclined at 45° to the surface of the single crystal. In the next stage, dislocation activation is reported[68] to occur on secondary slip planes. These slip planes must be oriented at 90° to the surface. The dislocation activation eventually leads to crack initiation by dislocation pileup. At higher loads, concurrent occurrences of both crack propagation and dislocation multiplication happen in this material.[68] In addition, the dislocations are reported to become mobile across suitable slip planes[68] of the

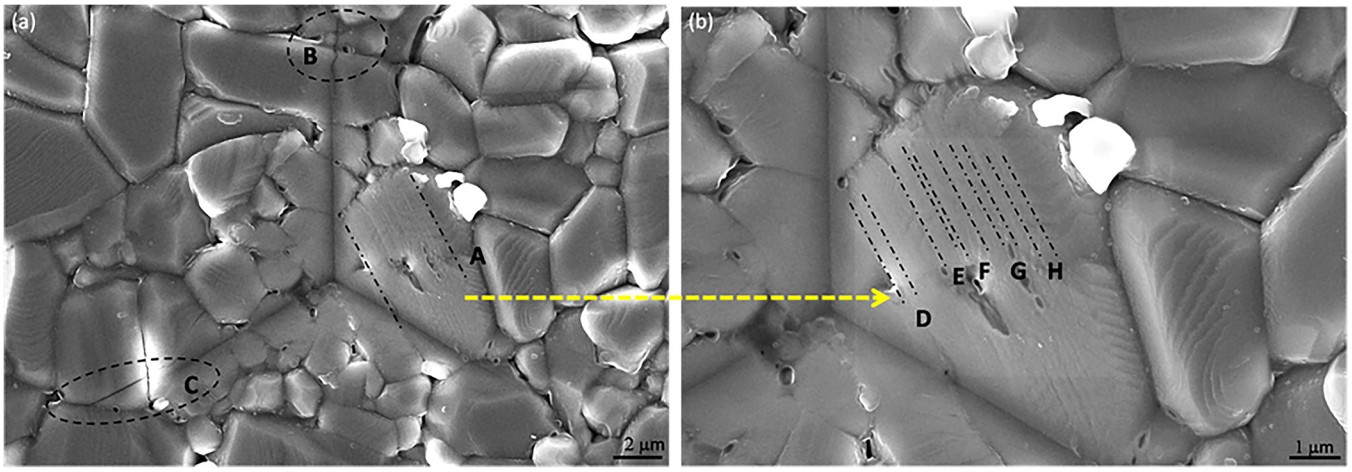

FIG. 11. FESEM images of (a) NI cavity showing shear deformation band formation (marked as "A" by black dotted lines) and microcracking formations at/near the two vertices of the nanoindents (marked as "B" and "C") inside the NI cavity at loading rate 33.33 mN s^{-1} for TDA 1 ceramics. (b) Exploded view of the region "A" showing five shear bands (marked as region "D," "E," "F," "G," and "H").

$SrTiO_3$ single crystal. To the best of our knowledge, there is no other report available. *Therefore, it seems plausible to argue that the quantitative contributions of shear deformation bad formation and microcrack formation to the nanoscale events in ceramics in general and the TDA ceramics, in particular, should constitute the scope of future study in this arena.*

10. Stochastic nature of the NSP events

The intrinsically stochastic nature of the NSP events, e.g., micro-pop-in is amply evidenced for NI of (100) as well as (111) surfaces of BCC Fe and (100) of FCC Cu,[63] Fe and Ta,[64] A-, C-, R-, and M-planes of single crystal alumina,[65] (110) surface of single crystal Pt,[69] and Zr-based metallic glass.[70] *The uniqueness of the current observation of the NSP events is that unlike load controlled NI*[63–65,69,70] *on single crystal materials, the current experiments are loading rate controlled and are on polycrystalline alumina pressureless sintered with TiO_2 as the sintering aid to assist densification.* For the sake of brevity, as typical illustrative examples, the frequency distributions and cumulative probabilities of the critical load (P_c) are shown in Fig. 15 for the TDA1 ceramics. Similar data for the TDA 3 and TDA 5 ceramics are shown, in turn, in Figs. S5

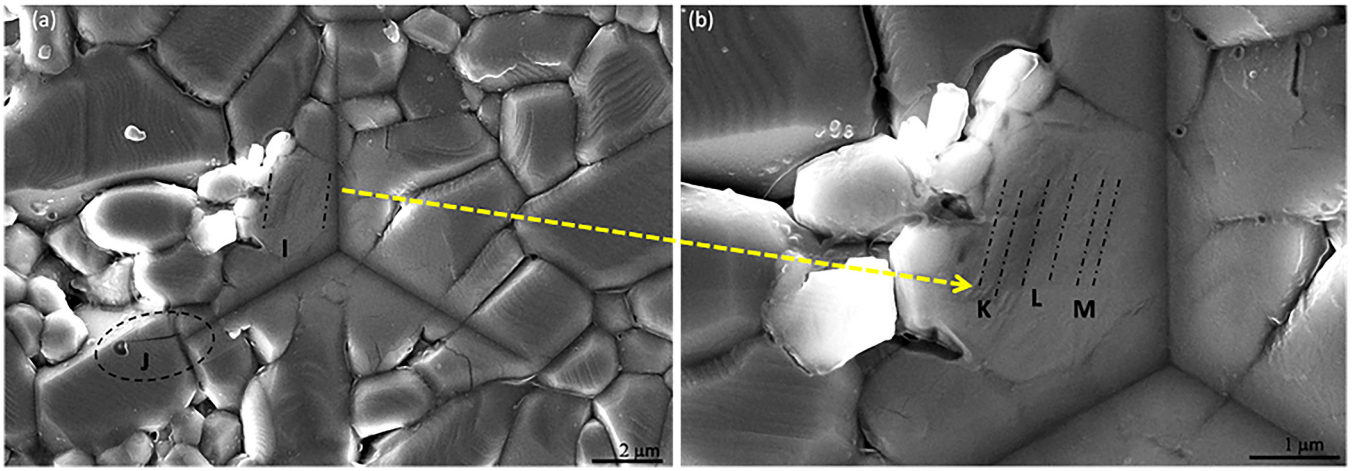

FIG. 12. FESEM images of (a) NI cavity showing shear deformation band formation (marked as "I" by black dotted lines) and microcracking formations at the bottom corner of the nanoindents (marked as "J" inside the NI cavity at loading rate 33.33 mN s^{-1} for TDA 3 ceramics). (b) Exploded view of the region "I" showing three shear bands (marked as region "K," "L," and "M").

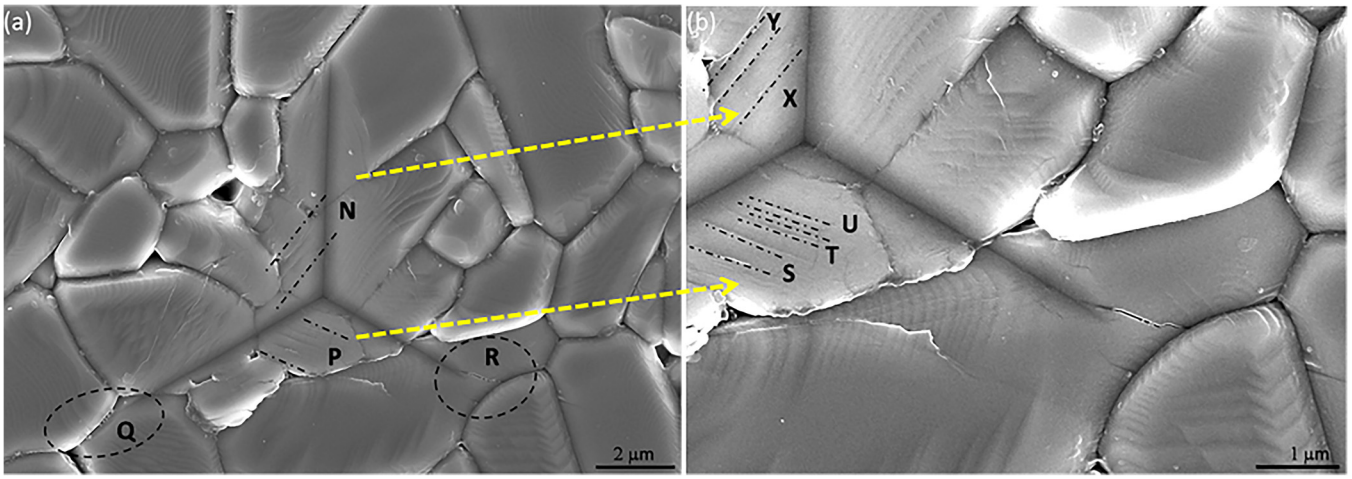

FIG. 13. FESEM images of (a) NI cavity showing shear deformation band formations (marked as "N" and "P" by black dotted lines) and microcracking formations at the bottom corners of the nanoindents (marked as "Q" and "R" inside the NI cavity at loading rate 33.33 mN s^{-1} for TDA 5 ceramics). (b) Exploded view of the region "P" showing three shear deformation bands (marked as "S," "T," and "U") and the region "N" showing two shear deformation bands (marked as "X" and "Y").

and S6 in the supplementary material. In all the cases, the loading rates of 1, 10, 33.3, and 500 mN s^{-1} are utilized as typical illustrative examples to depict the comparison of the stochastic natures of the NSP events.

All the P_c values exhibit a Gaussian distribution, as expected (Figs. 15, S5, and S6 in the supplementary material). A similar distribution is reported for the mean contact stress at the first pop-in in the cases of the A-, R-, C-, and M-planes of single crystal alumina.[65] Furthermore, these data trends are similar to those reported in the literature for a wide variety of materials[63,64,69,70] including those reported for single crystal alumina.[65,66]

It is interesting to note that for the TDA 1 ceramics, the range of P_c values at the first micro-pop-in is ≈0.10–0.18 mN at 1 mN s^{-1}, ≈0.10–0.18 mN at 10 mN s^{-1}, ≈0.13–0.21 mN at 33.3 mN s^{-1}, and ≈3.2–4.0 mN at 500 mN s^{-1} loading rates [Figs. 15(a)–15(d)]. Similarly, for the TDA 3 ceramics, the range of P_c values at the first micro-pop-in are ≈0.08–0.15 mN at 1 mN s^{-1}, ≈0.08–0.16 mN at 10 mN s^{-1}, ≈0.15–0.23 mN at 33.3 mN s^{-1}, and ≈3.7–4.5 mN at 500 mN s^{-1} loading rates [Figs. S5(a)–S5(d) in the supplementary material]. In a similar manner, for the TDA 5 ceramics, the range of P_c values at the first micro-pop-in are ≈0.09–0.17 mN at 1 mN s^{-1}, ≈0.10–0.18 mN at 10 mN s^{-1}, ≈0.23–0.31 mN at 33.3 mN s^{-1}, and ≈3.8–4.6 mN at 500 mN s^{-1} loading rates [Figs. S6(a)–S6(d) in the supplementary material]. These facts confirm that the range of P_c values enhance with loading rates. The enhancements become more noticeable at the loading rates equal to or greater than the threshold loading rate of 33.3 mN s^{-1} for all the TDA ceramics. These results also imply a similar nature of variation in the corresponding critical depth values as they are controlled mainly by the critical load values. Further, for a given loading rate, the range slightly increases with enhancement in the amount of sintering aid [Figs. 15, S5, and S6 in the supplementary material]. Furthermore, the ranges have wide statistical variation. The wide variation in contact stress at first pop-in in the A-, R-, C-, and M-planes of even single crystal alumina is attributed[65] to the statistical distribution of omnipresent surface defects and sub-surface defects induced in the damage zone beneath the NI. A similar logic may hold good here because the chances of having omnipresent surface defects and sub-surface defects induced in the damage zone beneath the NI is much more in the case of the polycrystalline TDA ceramics than in the case of single crystal alumina.

In recent studies,[65,66] spherical nanoindenter tips are used on single crystal alumina, mainly in load controlled NI experiments. However, the current study uses only a sharp Berkovich tip in loading rate controlled experiments conducted on the polycrystalline TDA ceramics. Therefore, a direct comparison of the data obtained in the present work with those from the literature[65,66] is not meaningful. But keeping in mind the overwhelming importance of the issue, a qualitative discussion is most desired. The same is given below.

As far as the mechanism is concerned, it has been suggested[65] that *individual twin deformation as well as cracking but not homogeneous nucleation of dislocations may lead to the* first pop-in that happens in the A-, C-, R-, and M- planes of single crystal alumina. In this case, a spherical nanoindenter with a tip radius of 2.95 μm is mostly used, except for one specific case, where a spherical nanoindenter of 0.6 μm is utilized.

On the contrary, other researchers[66] opine that when the nanoindenter tip radius of the spherical nanoindenter is sufficiently small (e.g., about 100 nm), the maximum shear stress may locally reach a magnitude equal to or greater than the shear strength, and hence, can induce homogeneous nucleation, multiplication, and movement of dislocations in single crystal alumina. It is suggested further[66] that at higher loads, dislocation pileup just underneath the nanoindenter can cause microcrack formation. On the other hand, for a situation when the nanoindenter tip radius of the

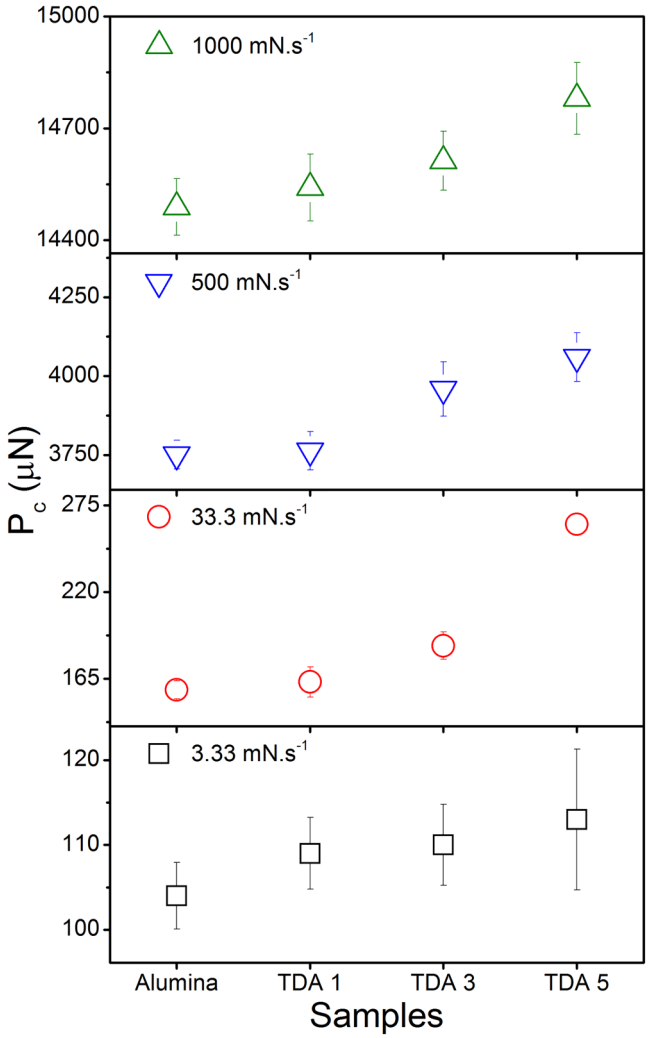

FIG. 14. The variations of critical load (P_c) with the amount of TiO_2 as a sintering aid in alumina ceramics for the typical applied loading rates of 3.33, 33.3, 500, and 1000 mN s^{-1}.

spherical nanoindenter is sufficiently large (e.g., about 2 μm), both dislocation induced NSP events and microcrack formations occur.[66]

Thus, the present observations (Figs. 5–15 and S1–S6 in the supplementary material) of the NSP events at loading rates of 1–1000 mN s^{-1} and microcrack formation at higher loading rate (e.g., 33.3 mN s^{-1}) in the NI experiments conducted with a sharp Berkovich tip of about 150 nm tip radius appear to be having features similar to what has been reported for single crystal alumina under different experimental conditions.[65,66] Therefore, based on the experimental data obtained from the present study and literature evidence,[65,66] it is proposed that both shear deformation band formation and microcrack formation can contribute to the occurrence of the NSP events expressed through micro-pop-ins in the P–h plots of the TDA ceramics. It is suggested further on the basis of current observations that the apparent contradiction about the mechanisms of pop-in as described in Ref. 65 and as described in Ref. 66 may be rationalized on the basis of enhancement in nanoindenter tip radius and hence the contact stress. However, further well-controlled definitive experiments which are beyond the scope of the present study will have to be done in future to check out the validity of the current propositions.

11. Theoretical justification of NSP: The broader theoretical perspective

Concurrent to experimental studies on NI, a huge amount of effort is directed globally to theoretically[71–88] understand the broader and intricate details of the NSP events in a wide variety of materials including single crystals, metals, thin films and multilayers, BMGs, metallic alloys, semiconductors, and ceramics. These data from the literature are presented in Table IV. The major theoretical approaches involve Finite Element Modeling (FEM),[71–76] Molecular Dynamic (MD) simulation,[77–80] DFT simulation,[81] a combination of both FEM and MD simulations,[82,83] DFT and MD,[84] as well as elastic contact mechanics, theories of dislocation, and plasticity.[85–88] The FEM approaches in various materials[71,72,75,76] including ceramics[73] confirm that micro-pop-ins happen mainly due to homogeneous and/or heterogeneous dislocation nucleation possibilities when $\tau_{max} \geq \tau_{theo}$. To the contrary, the MD simulations[77–80] suggest that the first or successive pop-ins largely depends on the tip radius and lattice resistance. The first pop-in occurs at stress close to τ_{CRSS} and successive pop-in happen due to the increment of heterogeneous dislocation nucleation.[78] However, the genesis of dislocation is opined to be directly linked to the structural changes.[80] On the other hand, when both the FEM and MD simulations are used for single crystals,[82,83] the τ_{max} values predicted by Hertzian contact mechanics are smaller than those estimated from the FEM simulation. The DFT and MD simulations[84] done in the cases of metals, BMGs, and semiconductors predict that pop-ins are related to lattice defects and generally occur at high stress $\sim \tau_{theo}$. On the contrary, elastic contact mechanics and plasticity theories[85–88] predict that pop-in occurs mainly due to homogeneous dislocation nucleation possibilities when $\tau_{max} \geq \tau_{theo}$. It is evident that in spite of the wealth of the literature,[70–88] further study is needed to bring more unequivocal clarity to the related issues.

In the case of ceramics, several researchers[32,38–40,65,66] report concurrent observation on both the NSP events and microcrack formation. The FEM simulation predicts that the pop-in occurs due to intense shear for Al/SiC thin films and multilayers.[72] In the case of yttrium aluminum garnet transparent ceramics,[73] the NSP events are predicted to be associated with homogeneous and/or heterogeneous dislocation nucleation possibilities when $\tau_{max} \geq \tau_{theo}$. The MD simulation predicts that the slip systems of pyramidal planes are mainly responsible for pop-in occurrence in GaN single crystals.[79] In the case of TiN single crystal, the DFT simulation[81] predicts that full dislocation nucleation occurs at $\tau \sim 6.7$ GPa. It is interesting to note that in the case of a-SiC thin films[86] pop-in is predicted by elastic contact mechanics and plasticity theories are to

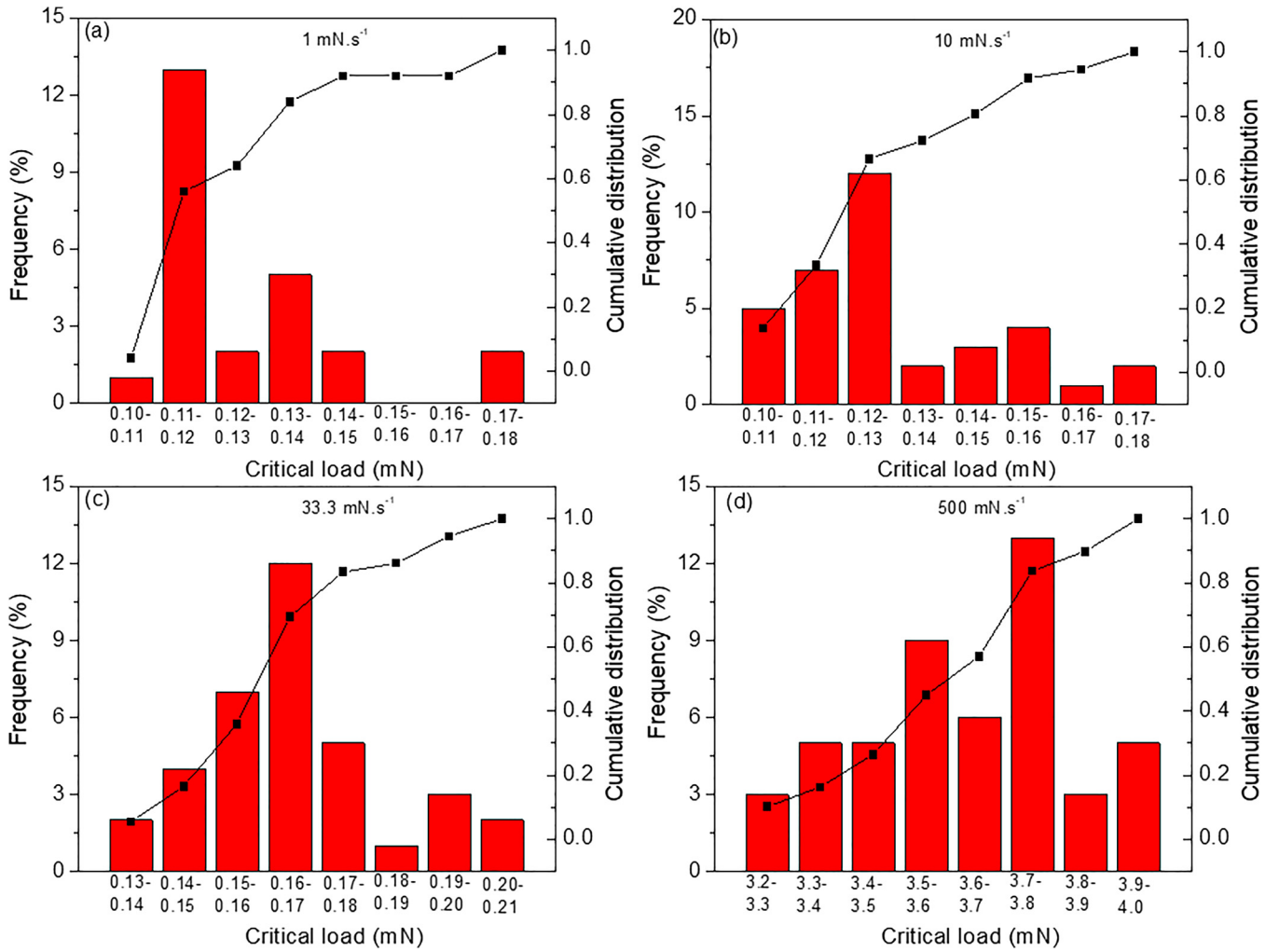

FIG. 15. The frequency distributions as well as cumulative probabilities of the critical load (P_c) of TDA 1 ceramics for loading rates of (a) 1, (b) 10, (c) 33.3, and (d) 500 mN s^{-1}.

be linked to the rearrangement of small local clusters of Si and C atoms. On the other hand, in the cases of 4H-SiC single crystal[87] and 3c-SiC thin films,[88] Hertzian contact mechanics and Johnson cavity models suggest that pop-in occurs mainly due to homogeneous dislocation nucleation possibilities when $\tau_{max} \geq \tau_{theo}$. But, the percentage of formation of shear deformation band and microcrack formation for pop-in are not exactly mentioned in any of the available reports (Table IV).[71–88]

Similar simulations are beyond the scope of the present work but will definitely constitute a major point of our future research effort. Based on the aforementioned literature[71–88] and experimental evidences obtained from the current study (Figs. 5–15 and S1–S6 in the supplementary material), it seems plausible to suggest that pop-in occurrence at lower loading rates is linked mainly to homogeneous nucleation of dislocation as τ_{max} is $\gg \tau_{theo}$. The same situation pertains even more vigorously at higher loading rates because of a higher rate of localized energy dissipation from the loading train to the TDA ceramics. Therefore, especially at higher loading rates the micro-pop-ins happen by the simultaneous occurrence of homogeneous dislocation nucleation, shear deformation band formations and microcrack formations inside the NI cavity. However, further studies are necessary to get a more clear view of the micro-pop-in events which characterize the NSP events in the present TDA ceramics.

12. Design implications of the current observations

The current study raises a futuristic design implication for development of both local deformation resistant and high strain rate resistant ceramic materials. This is how it happens. The

TABLE IV. Literature scenario for the occurrence of NSP events through simulations.

Materials	Load	Depth	Method	Remarks	Reference
C_{60} single crystal	0.2 mN		Finite element analysis	Pop-in event is due to homogeneous dislocation nucleation	71
Al/SiC thin-film multilayers		0.1–0.6 μm	Finite element models	Plasticity occurs due to intense shear	72
Yttrium aluminum garnet ceramics	2–10 mN		Finite element simulation	Pop-in is associated with homogeneous and/or heterogeneous dislocation nucleation possibilities when $\tau_{max} \geq \tau_{theo}$	73
SiC-6H single crystals	500 mN		Finite element simulation	Pop-in happens when $\tau_{max} \geq \tau_{theo}$ for the basal slip system	74
Mg alloys	5 mN		Crystal plastic finite element method (CPFEM)	The shear stress shows a lower level for twinning during (10–10) indentation compared to (1–210) indentation	75
Polycrystalline pure iron	1 mN		Finite element simulation	Homogeneous dislocation nucleation, grain boundaries, and surface roughness are responsible for plastic deformation	76
Model metallic glass	80 nN/nm		MD simulation	The cavitation stress is found to be reduced by the shear band deformation	77
Mo and Ni single crystal	1 and 0.4 μN		MD simulation	The first or successive pop-ins largely depends on the tip radius and lattice resistance. The first pop-in occurs at stress close to τ_{CRSS} and successive pop-in happens due to the increment of heterogeneous dislocation nucleation	78
GaN single crystal		2.2 nm	MD simulation	Slip systems of pyramidal planes are mainly responsible for pop-in	79
Cu thin films	1.4 nm		MD simulation	The genesis of dislocation is opined to be directly linked to the structural changes	80
TiN	*In situ* nanoindentation		DFT simulation	Full dislocation nucleation occurs at $\tau \sim 6.7$ GPa	81
Cu single crystal		5.03 nm	Finite element method and MD simulation	FEM simulations provide more realistic stress than using a simple shear stress state beneath the nanoindenter	82
Tungsten crystals	700 μN		Finite element simulation and MD simulation	τ_{max} values predicted by Hertzian contact mechanics are smaller than those estimated from FEM simulation	83
Metals, semiconductors, and BMGs	1 mN		DFT and MD simulation	Pop-ins are related to lattice defects and generally occur at high stress $\sim \tau_{theo}$	84
Pd-based and Zr-based BMG	20 N		Elastic Volterra's theory of dislocation	Elastic fields near the shear band are associated with the Volterra-type macro-dislocation	85
a-SiC thin film	0.05–3 mN		Hertzian contact theory and Johnson's cavity model	Pop-in is linked to rearrangement of small local clusters of Si and C atoms	86
Single crystal 4H-SiC	0.9–9 mN		Hertzian contact theory and Johnson's cavity model	Pop-in occurs mainly due to homogeneous dislocation nucleation possibilities when $\tau_{max} \geq \tau_{theo}$	87
3C-SiC thin film	0.5–5 mN		Johnson cavity model	Dislocation nucleation is the actual reason for elastic to plastic deformation rather than tensile stresses	88

present results show the loading rate dependent (1–1000 mN s^{-1}) enhancement in nanohardness, Young's modulus, as well as critical load at first pop-in during nanoindentation of titania densified alumina (TDA) ceramics. Furthermore, the critical loads show a Gaussian distribution at all loading rates. Thus, it provides unmistakable evidence in favor of the intrinsically stochastic nature of the NSP events. Furthermore, the range of critical load enhance slightly with loading rate and the amount of titania used as the sintering aid. In addition, as more Titania sintering aid is used, the fine grain size is decreased simultaneously and the relative density is increased in the TDA ceramics. As a result, the microstructure provides more resistance to localized plastic deformation at the nanoscale. This is reflected as an enhancement in the critical load value to initiate plasticity events at the nanoscale as the loading rate is increased. This situation suggests that it should be possible to optimize the microstructure by choosing the appropriate amount of titania sintering aid. This is where the current study leads to two possibilities. The first one is the possibility of enhancement of the resistance against the contact induced deformation at the microstructural length scale. The second one is the possibility to enhance the resistance at the microstructural length scale against rapid change in loading rate. The simultaneous achievements of these two possibilities in the current study indicate the possibility of tuning the microstructure of alumina ceramics by the variation of the amount of TiO_2 as the sintering aid. Such simple microstructural tuning of highly dense TDA ceramics may be used to design materials for both local deformation resistant and high strain rate resistant applications in future.

IV. CONCLUSIONS

The major conclusions of the present study are as follows.

There is undeniable experimental evidence that loading rate ($\dot{P} \approx 1$–1000 mN s^{-1}) dependent NSP events, characterized by profuse serration and micro-pop-ins in the load-depth plots obtained during NI experiments conducted with a diamond Berkovich nanoindenter, happen in alumina ceramics pressureless sintered with 1, 3, and 5 wt. % of titania (e.g., the TDA ceramics). Both nanohardness and Young's modulus enhance with loading rate ($\dot{P}$). Almost all the micro-pop-in related parameters, e.g., (P_c), (h_c), (ΔP), (Δh), (τ_{max}), (ρ_D), and (τ_{CRSS}), also enhance exhibiting empirical power law dependencies on ($\dot{P}$) with a positive exponent. These observations are justified from both qualitative argument and theoretical simplistic modeling. As the critical loads at the first micro-pop-in show a Gaussian distribution at all loading rates, it confirms the intrinsically stochastic nature of the NSP events. The range of critical loads enhance slightly with ($\dot{P}$) and the amount of titania used as the sintering aid, presumably due to a simultaneous reduction in the fine grain size and an enhancement of the relative density in the TDA ceramics. Analysis of the experimental data obtained from the (NI) experiments and extensive study of the NI cavity by the FESEM technique at especially high loading rate suggest that homogeneous dislocation nucleation under the nanoindenter, shear deformation band formation, and microcrack formation can contribute to the occurrence of the NSP events. Hence, the utilization of TiO_2 as a sintering aid provides a unique and novel technique to tune and optimize the alumina microstructure for loading rate dependent enhancement of nanohardness and resistance against contact induced deformation at the nanoscale. In the future, such optimization may provide advanced alumina ceramics for prospective real life applications, e.g., impact resistant tiles, impact resistant coatings, and armor tiles.

SUPPLEMENTARY MATERIAL

See the supplementary material for the table containing the compositions of the samples (Table S1), variations of P_c, corresponding h_c, ΔP, and Δh with (dP/dt) for TDA 3 (Fig. S1) and TDA 5 (Fig. S3) ceramics, variations of (τ_{max}), (ρ_D) per unit area, (R_D), and (τ_{CRSS}) with (dP/dt) in the case of TDA 3 (Fig. S2) and TDA 5 (Fig. S4) ceramics, the empirical power law equations of micro-pop-in parameters for TDA 3 (Table S2) and TDA 5 (Table S3) ceramics, the frequency distributions, as well as cumulative probabilities of the critical load (Pc) for TDA 3 (Fig. S5) and TDA 5 (Fig. S6) ceramics.

ACKNOWLEDGMENTS

All authors acknowledge the Director, CSIR—Central Glass and Ceramic Research Institute (CSIR-CGCRI), Kolkata 700032, India for allowing them to carry out the experiments and publish the paper. All authors also thank Mr. S. K. Dalui, Senior Technical Officer, AMCCD, CSIR-CGCRI for his continuous help during NI experiments. Finally, Ms. Payel Maiti acknowledges the DST INSPIRE fellowship scheme, Government of India (Grant No. DST/INSPIRE Fellowship/2016/IF160102) for financial support.

AUTHOR DECLARATIONS

Conflict of Interest

The authors have no conflicts to disclose.

DATA AVAILABILITY

The data that support the findings of this study are available from the corresponding authors upon reasonable request.

REFERENCES

[1] Y. Liu, X. Cui, R. Niu, S. Zhang, X. Liao, S. D. Moss, P. Finkel, M. Garbrecht, S. P. Ringer, and J. M. Cairney, Nat. Commun. **13**, 335 (2022).
[2] F. Bouville and A. R. Studart, Nat. Commun. **8**, 14655 (2017).
[3] Q. An, K. M. Reddy, J. Qian, K. J. Hemker, M. W. Chen, and W. A. Goddard III, Nat. Commun. **7**, 11001 (2016).
[4] A. Taloni, M. Vodret, G. Costantini, and S. Zapperi, Nat. Rev. Mater. **3**, 211 (2018).
[5] X. Ke, J. Ye, Z. Pan, J. Geng, M. F. Besser, D. Qu, A. Caro, J. Marian, R. T. Ott, Y. M. Wang, and F. Sansoz, Nat. Mater. **18**, 1207 (2019).
[6] X. Li, L. Lu, J. Li, X. Zhang, and H. Gao, Nat. Rev. Mater. **5**, 706 (2020).
[7] A. Rosenflanz, M. Frey, B. Endres, T. Anderson, E. Richards, and C. Schardt, Nature **430**, 761 (2004).
[8] S. Pathak, S. R. Kalidindi, J. S. Weaver, Y. Wang, R. P. Doerner, and N. A. Mara, Sci. Rep. **7**, 11918 (2017).
[9] N. Li, H. Wang, A. Misra, and J. Wang, Sci. Rep. **4**, 6633 (2014).
[10] T. Fu, X. Peng, C. Huang, H. Xiang, S. Weng, Z. Wang, and N. Hu, Sci. Rep. **7**, 4768 (2017).
[11] S. Kondo, A. Ishihara, E. Tochigi, N. Shibata, and Y. Ikuhara, Nat. Commun. **10**, 2112 (2019).

[12]H. Yang, H. Fang, H. Yu, Y. Chen, L. Wang, W. Jiang, Y. Wu, and J. Li, Nat. Commun. **10**, 854 (2019).
[13]O. F. Dippo, N. Mesgarzadeh, T. J. Harrington, G. D. Schrader, and K. S. Vecchio, Sci. Rep. **10**, 21288 (2020).
[14]B. M. Moshtaghioun, F. L. Cumbrera, D. Gómez-García, and J. I. Peña, Sci. Rep. **9**, 13340 (2019).
[15]E. Zalnezhad, F. Musharavati, T. Chen, F. Jaber, K. Uzun, M. E. H. Chowdhury, A. Khandakar, J. Liu, and S. Bae, Sci. Rep. **11**, 1867 (2021).
[16]M. Mirkhalaf, H. Yazdani Sarvestani, Q. Yang, M. B. Jakubinek, and B. Ashrafi, Sci. Rep. **11**, 6951 (2021).
[17]L. Zorzetto, L. Andena, F. Briatico-Vangosa, L. De Noni, J.-M. Thomassin, C. Jérôme, Q. Grossman, A. Mertens, R. Weinkamer, M. Rink, and D. Ruffoni, Sci. Rep. **10**, 22285 (2020).
[18]W. Huang, M. Shishehbor, N. Guarín-Zapata, N. D. Kirchhofer, J. Li, L. Cruz, T. Wang, S. Bhowmick, D. Stauffer, P. Manimunda, K. N. Bozhilov, R. Caldwell, P. Zavattieri, and D. Kisailus, Nat. Mater. **19**, 1236 (2020).
[19]S. B. Roshni, M. T. Sebastian, and K. P. Surendran, Sci. Rep. **7**, 40839 (2017).
[20]S. Conze, M. Grimm, L.-M. Berger, S. Thiele, R. Drehmann, and T. Lampke, Surf. Coat. Technol. **405**, 126702 (2021).
[21]V. T. d. S. Aragao, V. S. Silva, R. R. de Carvalho, R. S. Matos, N. S. Ferreira, D. M. d. A. Melo, and R. M. P. B. Oliveira, J. Mater. Res. Technol. **15**, 2711 (2021).
[22]L. Łatka, M. Michalak, M. Szala, M. Walczak, P. Sokołowski, and A. Ambroziak, Surf. Coat.Technol. **410**, 126979 (2021).
[23]K. Shigeno, M. Li, and H. Fujimori, J. Eur. Ceram. Soc. **41**, 376 (2021).
[24]M. Daniel Barros, H. Jellito, D. Hotza, and R. Janssen, J. Am. Ceram. Soc. **104**, 1047 (2021).
[25]O. P. Oladijo, A. P. I. Popoola, M. Booi, J. Fayomi, and L. L. Collieus, S. Afr. J. Chem. Eng. **33**, 58 (2020).
[26]H. Manshor, E. C. Abdullah, A. Z. A. Azhar, Y. W. Sing, and Z. A. Ahmad, J. Alloys Compd. **722**, 458 (2017).
[27]Y. Sui, L. Han, and Y. Jiang, Ceram. Int. **44**, 14811 (2018).
[28]M. M. S. Wahsh, R. M. Khattab, and M. F. Zawrah, Mater. Res. Bull. **48**, 1411 (2013).
[29]C.-J. Wang and C.-Y. Huang, Mater. Sci. Eng. A **492**, 306 (2008).
[30]T. Bai and T. Xie, J. Alloys Compd. **745**, 562 (2018).
[31]M. Bhattacharya, A. Dey, and A. K. Mukhopadhyay, Mater. Res. Express **3**, 045017 (2016).
[32]M. Bhattacharya, R. Chakraborty, A. Dey, A. Kumar Mandal, and A. Kumar Mukhopadhyay, Ceram. Int. **39**, 999 (2013).
[33]W. Mao and Y. Shen, J. Am. Ceram. Soc. **95**, 3605 (2012).
[34]M. Bhattacharya, A. Dey, and A. K. Mukhopadhyay, Ceram. Int. **42**, 13378 (2016).
[35]W. G. Mao, Y. G. Shen, and C. Lu, Scr. Mater. **65**, 127 (2011).
[36]J. Gong, Z. Peng, and H. Miao, J. Eur. Ceram. Soc. **25**, 649 (2005).
[37]P. Maiti, A. Eqbal, M. Bhattacharya, P. S. Das, J. Ghosh, and A. K. Mukhopadhyay, Ceram. Int. **45**, 8204 (2019).
[38]P. Maiti, M. Bhattacharya, P. S. Das, J. Ghosh, and A. K. Mukhopadhyay, Ceram. Int. **45**, 25034 (2019).
[39]P. Maiti, J. Ghosh, and A. K. Mukhopadhyay, Ceram. Int. **46**, 3144 (2020).
[40]P. Maiti, J. Ghosh, and A. K. Mukhopadhyay, Ceram. Int. **47**, 9090 (2021).
[41]J. Amodeo, E. Maras, and D. Rodney, npj Comput. Mater. **7**, 60 (2021).
[42]W. C. Oliver and G. M. Pharr, J. Mater. Res. **19**, 3 (2004).
[43]H. Shang, T. Rouxel, M. Buckley, and C. Bernard, J. Mater. Res. **21**, 632 (2006).
[44]C. E. Packard and C. A. Schuh, Acta Mater. **55**, 5348 (2007).
[45]T. F. Page, W. C. Oliver, and C. J. McHargue, J. Mater.Res. **7**, 450 (1992).
[46]J. W. Morris, *Encyclopedia of Materials: Science and Technology* (Elsevier Science, Amsterdam, 2001).
[47]A. Gouldstone, H. J. Koh, K. Y. Zeng, A. E. Giannakopoulos, and S. Suresh, Acta Mater. **48**, 2277 (2000).
[48]M. Bhattacharya, R. Chakraborty, A. Dey, A. K. Mandal, and A. K. Mukhopadhyay, Appl. Phys. A **107**, 783 (2012).
[49]X. P. Zhao, J. B. Yin, L. Q. Xiang, and Q. Zhao, J. Mater. Sci. **37**, 2569 (2002).
[50]H. Bei, Y. F. Gao, S. Shim, E. P. George, and G. M. Pharr, Phys. Rev. B **77**, 060103(R) (2008).
[51]V. V. Brazhkin, A. G. Lyapin, and R. J. Hemley, Philos. Mag. A **82**, 231 (2002).
[52]A. Nakamura, K. P. D. Lagerlöf, K. Matsunaga, J. Tohma, T. Yamamoto, and Y. Ikuhara, Acta Mater. **53**, 455 (2005).
[53]A. H. Heuer, K. P. D. Lagerlöf, and J. Castaing, Philos. Mag.A **78**, 747 (1998).
[54]M. Huráková, K. Csach, A. Juríková, J. Miškuf, Š Demčák, V. Ocelík, and J. T. M. De Hosson, J. Non-Cryst. Solids **470**, 160 (2017).
[55]S. J. Bull, T. F. Page, and E. H. Yoffe, Philos. Mag. Lett. **59**, 281 (1989).
[56]D. Trejo-Arroyo, J. Zárate-Medina, J. M. Alvarado-Orozco, M. E. Contreras-García, M. S. Boldrick, and J. Muñoz-Saldāna, J. Eur. Ceram. Soc. **33**, 1907 (2013).
[57]M. Bhattacharya, "Department of Physics," Ph.D. dissertation (Jadavpur University, 2016).
[58]C. A. Schuh, T. C. Hufnagel, and U. Ramamurty, Acta Mater. **55**, 4067 (2007).
[59]S. N. Dub, V. V. Brazhkin, N. V. Novikov, G. N. Tolmachova, P. M. Litvin, L. M. Lityagina, and T. I. Dyuzheva, J. Superhard Mater. **32**, 406 (2010).
[60]N. I. Tymiak, A. Daugela, T. J. Wyrobek, and O. L. Warren, Acta Mater. **52**, 553 (2004).
[61]S. Lahiri, S. Sinhamahapatra, H. S. Tripathi, and K. Dana, Ceramic. Int. **42**, 15405 (2016).
[62]T. Ebisu and S. Horibe, J. Eur. Ceram. Soc. **30**, 2419 (2010).
[63]Y. Sato, S. Shinzato, T. Ohmura, T. Hatano, and S. Ogata, Nat. Commun. **11**, 4177 (2020).
[64]Y. Sato, S. Shinzato, T. Ohmura, and S. Ogata, Int. J. Plast. **121**, 280 (2019).
[65]Y. Ma, L. Cao, W. Hang, T. Zhang, and J. Yuan, Ceram. Int. **46**, 15554 (2020).
[66]X. Fang, H. Bishara, K. Ding, H. Tsybenko, L. Porz, M. Höfling, E. Bruder, Y. Li, G. Dehm, and K. Durst, J. Am. Ceram. Soc. **104**, 4728 (2021).
[67]B. Bor, D. Giuntini, B. Domènech, M. V. Swain, and G. A. Schneider, J. Eur. Ceram. Soc. **39**, 3247 (2019).
[68]X. Fang, K. Ding, C. Minnert, A. Nakamura, and K. Durst, J. Mater. Sci. **56**, 5479 (2021).
[69]C. A. Schuh, J. K. Mason, and A. C. Lund, Nat. Mater. **4**, 617 (2005).
[70]Y. Yang, X. L. Fu, S. Wang, Z. Y. Liu, Y. F. Ye, B. A. Sun, and C. T. Liu, Sci. Rep. **4**, 6699 (2014).
[71]S. N. Dub, C. Haftaoglu, and V. M. Kindrachuk, J. Mater. Sci. **56**, 10905 (2021).
[72]S. Bigelow and Y. L. Shen, Front. Mater. **4**, 25 (2017).
[73]H. Wang, R. Li, M. Zhou, J. Cedelle, Z. Huang, and Q. Wang, J. Eur. Ceram. Soc. **37**, 2705 (2017).
[74]A. Datye, L. Li, W. Zhang, Y. Wei, Y. Gao, and G. M. Pharr, J. Appl. Mech. **83**, 091003 (2016).
[75]J. Cheng, "Institute for frontier materials," Ph.D. dissertation (Deakin University, 2019).
[76]F. Pohl, Sci. Rep. **9**, 15350 (2019).
[77]Y. Yang, J. Luo, L. Huang, G. Hu, K. D. Vargheese, Y. Shi, and J. C. Mauro, Acta Mater. **115**, 413 (2016).
[78]Y. Xia and H. Bei, J. Mater. Res. **31**, 2065 (2016).
[79]Y. Qian, F. Shang, Q. Wan, and Y. Yan, J. Appl. Phys. **124**, 115102 (2018).
[80]D. Chocyk and T. Zientarski, Adv. Sci. Technol. Res. J. **16**, 170 (2022).
[81]N. Li, S. K. Yadav, X. Y. Liu, J. Wang, R. G. Hoagland, N. Mara, and A. Misra, Sci. Rep. **5**, 15813 (2015).
[82]T. Zhu, J. Li, K. J. VanVliet, S. Ogata, S. Yip, and S. Suresh, J. Mech. Phys. Solids **52**, 691 (2004).
[83]L. Ma, L. Levine, R. Dixson, D. Smith, and D. Bahr, J. Mater. Res. **22**, 1656 (2007).
[84]T. Ohmura and M. Wakeda, Materials **14**, 1879 (2021).
[85]M. Seleznev and A. Vinogradov, Metals **10**, 374 (2020).
[86]A. Nawaz, W. G. Mao, C. Lu, and Y. G. Shen, Ceram Int. **43**, 385 (2017).
[87]A. Nawaz, W. G. Mao, C. Lu, and Y. G. Shen, J. Mech. Behav. Biomed. Mater. **66**, 172 (2017).
[88]A. Nawaz, B. Islam, W. Mao, C. Lu, and Y. Shen, Appl. Ceram. Technol. **16**, 706 (2019).